Advances in Applied Biomaterials and Biocomposites
https://www.sciltp.com/journals/aabb

Review

Integration of NIR-II Functional Nanostructures for Cancer Theranostics

Ekram Hossain †, Jiaqi Liu †, Xiaomeng Zeng, Xingyu Guan, Zhenyu Wang * and Xiang Mao *

College of Biomedical Engineering, Chongqing Medical University, Chongqing 400016, China
* Correspondence: 203853@cqmu.edu.cn (Z.W.); maox@cqmu.edu.cn (X.M.)
† These authors contributed equally to this work.

How To Cite: Hossain, E.; Liu, J.; Zeng, X.; et al. Integration of NIR-II Functional Nanostructures for Cancer Theranostics. *Advances in Applied Biomaterials and Biocomposites* **2026**, *1*(1), 3.

Received: 16 January 2026
Revised: 8 April 2026
Accepted: 13 April 2026
Published: 14 April 2026

Abstract: The development of near-infrared II (NIR-II, 1000–1700 nm) technologies has opened new opportunities for biomedical applications, particularly in cancer diagnosis and therapy. Compared with conventional NIR-I systems (700–900 nm), NIR-II nanoplatforms offer deeper tissue penetration, reduced photon scattering, and minimal autofluorescence, enabling high-resolution, high-contrast imaging and improved therapeutic performance. A wide range of NIR-II-responsive nanostructures has been developed, including metal-based, carbon-based, semiconductor-based, hybrid/composite nanostructures, and organic fluorophores. These nanomaterials exhibit unique optical and physicochemical properties that support advanced applications such as fluorescence imaging (FLI), photothermal therapy (PTT), and photodynamic therapy (PDT), particularly in cancer theranostics. This review systematically summarizes recent advances and integration strategies of NIR-II functional nanostructures, with a particular focus on their roles in cancer imaging and image-guided therapy. However, key challenges associated with clinical translation including long-term toxicity, biodistribution, clearance, scalability, cost, and stability remain significant and are critically discussed. Finally, future perspectives are outlined, emphasizing the development of biocompatible, efficient, and clinically translatable NIR-II nanoplatforms.

Keywords: NIR-II nanoplatforms; functional structures; cancer theranostics; clinical translation

1. Introduction

Cancer remains one of the leading causes of death worldwide, necessitating the development of more precise diagnostic and therapeutic strategies [1]. In recent years, NIR-II technology has emerged as a promising platform for biomedical applications due to its superior tissue penetration, reduced photon scattering, and minimal autofluorescence compared to visible and NIR-I imaging [2]. These advantages enable high-resolution, deep-tissue imaging and more accurate tumor localization. NIR-II-responsive nanostructures, particularly metal-based, carbon-based, semiconductor-based, hybrid/composite and organic fluorophores have attracted significant attention for their multifunctional capabilities in FLI, PTT, and PDT [3–5]. Their unique optical properties allow real-time visualization of biological processes at the molecular and cellular levels, while also enabling efficient light-to-heat conversion for targeted cancer treatment. This capability is further supported by recent advances in optical probe design, including small-molecule fluorophores, semiconducting polymer nanoparticles, and aggregation-induced emission materials, which enable high-resolution, real-time monitoring of complex biological processes and enhance theranostic performance [6]. As a result, these nanoplatforms have shown promising potential in image-guided therapy, drug delivery, and disease diagnostics [7–9]. Importantly, the integration of imaging and therapeutic functionalities within a single NIR-II nanoplatform enables precise, image-guided treatment, significantly enhancing therapeutic accuracy

and clinical potential. However, conventional bioimaging and therapy techniques are still limited by tissue absorption, scattering, and autofluorescence from biological components such as hemoglobin and melanin, which reduce imaging clarity and penetration depth [10]. The NIR-II windows effectively overcomes these limitations, significantly improving imaging sensitivity and lesion detection, as demonstrated in recent studies. However, the clinical application of NIR-II imaging remains limited due to insufficient development of nanodrugs and technological constraints. In order to help patients with liver cancer during surgery, NIR-II fluorescence imaging was first published in 2019. An entirely new era in cancer diagnosis was ushered in when intraoperative studies showed that NIR-II FLI exhibited greater sensitivity and superior lesion recognition capacity when compared with imaging in visible and NIR-I areas [11]. In addition, PTT has attracted significant attention among various therapeutic methods, leveraging nanoparticles with high photothermal conversion efficiency (PCE) to induce cancer cell ablation by converting light energy into heat energy upon external excitation [12–16]. Among various therapeutic approaches, NIR-II based PTT has gained considerable interest due to its high specificity, minimal invasiveness, and controllable therapeutic effects [17]. They can efficiently convert light energy into heat, inducing cancer cell death while minimizing damage to surrounding normal tissues. Moreover, NIR-II-mediated PTT can be combined with other treatment modalities, such as chemotherapy and PDT, to enhance therapeutic outcomes [18,19]. NIR-II-based PTT has also demonstrated strong potential in improving therapeutic efficiency due to its superior tissue penetration [20–22]. Although combining NIR-II-mediated PTT with other therapeutic modalities has been shown to enhance therapeutic efficacy, effective application still requires high photothermal efficiency, low biological toxicity, and facile functionalization [23]. In recent years, a wide range of NIR-II nanomaterials including metal-based, carbon-based, semiconductor-based, hybrid/composite nanostructures, as well as organic fluorophores have demonstrated significant potential in biomedical applications [24–27]. These nanoplatforms enable dual laser-mediated therapeutic approaches within the NIR-II windows, particularly for both PTT and PDT. For instance, metal-based nanostructures (e.g., Pd, Au, Pt, Cu) exhibit favorable optical and photothermal properties, making them effective agents for drug delivery and phototherapy [28]. Meanwhile, carbon-based materials, semiconductor nanostructures, and organic fluorophores provide additional advantages such as tunable optical properties, improved biocompatibility, and structural versatility. Despite these advances, significant challenges including potential toxicity, high material cost, and limitations in large-scale production continue to hinder clinical translation. Therefore, continued efforts in rational material design, functional optimization, and biocompatibility enhancement are essential to fully realize the clinical potential of NIR-II-responsive nanomaterials. In this review, we systematically summarize recent advances in NIR-II-responsive nanostructures, with a focus on their design, optical properties, and cancer theranostics applications, including imaging, PTT, PDT, and synergistic therapeutic strategies.

2. Metal-Based NIR-II Nanomaterials

NIR-II-responsive nanomaterials can be broadly classified into metal-, carbon-, semiconductor-based, hybrid/composite systems, and organic fluorophores according to their composition and optical properties. Among these, pure-phase metal-based nanomaterials have attracted considerable attention due to their strong localized surface plasmon resonance (LSPR), high photothermal efficiency, and tunable optical absorption in the NIR-II windows. Compared with carbon-based and organic systems, metal-based nanomaterials generally exhibit higher photothermal efficiency, although they may raise greater concerns regarding long-term biocompatibility and clearance. These features make them promising candidates for cancer theranostics, including FLI, PTT, PDT, and imaging-guided treatment. However, their performance is highly dependent on composition, morphology, and surface engineering, highlighting the need for a more systematic evaluation of structure–property relationships.

2.1. Utilization of Gold-Based Materials for NIR-II Applications

Gold-based nanoparticles have been extensively explored across diverse fields due to their unique physicochemical and optical properties. In particular, they demonstrate significant potential in fluorescence imaging and nanogold labeling, attributed to their high electron density and tunable light scattering behavior. Various such nanostructures, including Au_3Cu alloys, tetrapod nanocrystals (TPNCs), and AuNPL@TiO_2, exhibit excellent biocompatibility, supporting their application in PTT. The key advantages of these nanomaterials include outstanding stability, facile surface functionalization, efficient photothermal efficiency, and tunable LSPR in the near-infrared region [29]. Collectively, these features position gold nanostructures as highly efficient light-to-heat transducers for cancer theranostics. Notably, the photothermal therapy of these nanomaterials is strongly governed by their morphology, size, and surface engineering, which directly influence LSPR behavior and light absorption in the NIR-II windows. For instance, Luo et al. (2020) developed a multifunctional nanosensitizer, GNRs@mSiO_2−EuBA/HP (GSE-HP), consisting of gold nanorods coated with mesoporous silica and loaded with

hematoporphyrin (HP) [30]. As illustrated in Figure 1A, GSE-HP functions as a photothermal agent (PTA), radiosensitizer, and photosensitizer carrier. The strong NIR absorption and high X-ray attenuation of gold nanostructures enable dual-modal photoacoustic (PA) and computed tomography (CT) imaging. The nanosystem exhibits dimensions of 57.1 ± 2.9 nm in length and 15.7 ± 1.4 nm in width, synthesized via a seed-mediated growth method. Importantly, the silica coating induces a red-shift in absorbance from 810 to 846 nm (Figure 1B), improving optical penetration. Under laser irradiation, GSE-HP demonstrates rapid temperature elevation (Figure 1C) and a high photothermal efficiency (η) of 38.4%, along with excellent photothermal stability. In vivo results further reveal significant tumor suppression, particularly in group 10 (GSE-HP + X + L), without noticeable body weight loss (Figure 1D) [31]. From a design perspective, this study highlights that core–shell architectures and dielectric coatings (e.g., SiO_2) play a crucial role in modulating optical absorption and enhancing photothermal stability, rather than relying solely on intrinsic gold properties. Similarly, Wang et al. (2018) synthesized Au_3Cu tetrapod nanocrystals (TPNCs) via a seed-mediated approach involving $HAuCl_4•3H_2O$, $CuCl_2•2H_2O$, and glucose [32]. The growth evolution is illustrated in Figure 1E, yielding tetrapods with an average arm length of 22.8 ± 4.6 nm and broad absorption spanning the NIR-I and NIR-II windows **(**Figure 1F). Surface modification with PEG derivatives (HS-PEG-NH_2, HS-PEGNH-FA, HE-PEGNH-Cy5) significantly improves water solubility, targeting capability, and biocompatibility, resulting in Au_3Cu@PEG TPNCs.

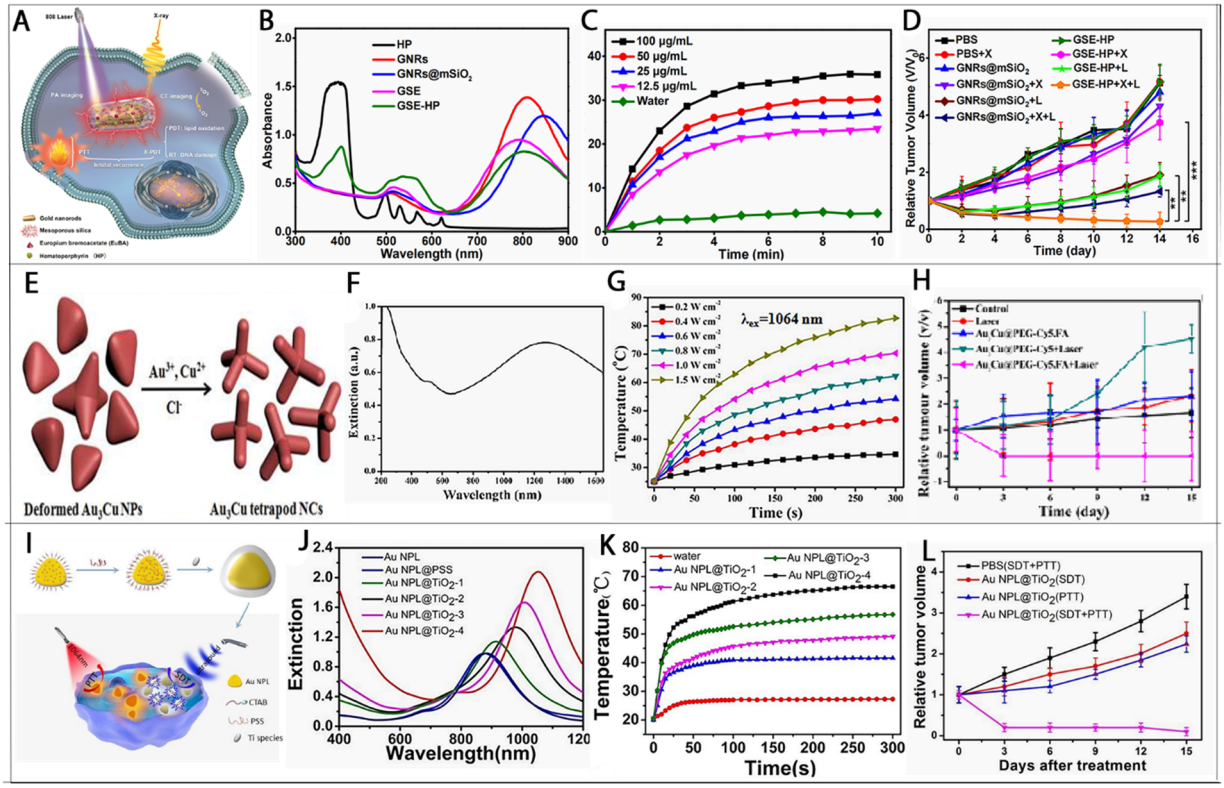

Figure 1. (**A**) Schematic illustration of the working mechanism of GSE-HP. (**B**) UV–vis absorption spectra of GSE-HP compared with control groups. (**C**) Photothermal heating profiles of GSE-HP dispersions under 808 nm laser irradiation at 0.8 W cm^{-2}. (**D**) Tumor growth curves in different treatment groups in tumor-bearing mice (Reprinted/adapted with permission from Ref. [30]. 2020, American Chemical Society). (**E**) Schematic representation of the formation process of Au_3Cu tetrapod nanocrystals. (**F**) UV–vis extinction spectrum of TPNCs. (**G**) Temperature elevation profiles of Au_3Cu@PEG TPNC dispersions under 1064 nm laser irradiation at different power densities (0.2–1.5 W cm^{-2}). (**H**) Tumor growth curves following different treatments in tumor-bearing mice (Reprinted/adapted with permission from Ref. [32]. 2018, The Royal Society of Chemistry). (**I**) Schematic illustration of AuNPL@TiO_2 synthesis and combined photothermal–sonodynamic therapy in HeLa cells. (**J**) UV–vis extinction spectra of conventional gold nanoplates and TiO_2-coated nanoplates with varying shell thicknesses. (**K**) Temperature profiles of AuNPL@TiO_2 after 5 min of 1064 nm laser irradiation (1 W cm^{-2}) with different shell thicknesses. (**L**) Tumor growth curves under different treatment conditions (Reprinted/adapted with permission from Ref. [33]. 2018, The Royal Society of Chemistry).

The Au_3Cu@PEG TPNCs exhibits a high mass extinction coefficient of 53 L g^{-1} cm^{-1} at 1064 nm, indicating strong NIR-II absorption. Under 1064 nm laser irradiation, rapid temperature elevation is observed within 5 min

(Figure 1G). In vivo studies demonstrate effective tumor suppression in the Au_3Cu@PEG-Cy5, FA + Laser group without affecting body weight (Figure 1H), confirming low systemic toxicity. Compared to conventional inorganic photothermal agents, Au_3Cu-based systems benefit from alloy-induced plasmonic coupling, which enhances light absorption across a broader spectral range. This suggests that bimetallic or alloyed nanostructures offer a promising strategy to extend LSPR into the NIR-II windows while improving photothermal efficiency through synergistic electronic interactions.

In addition to alloy systems, structural engineering also plays a critical role. Song et al. synthesized gold nanostars with strong NIR SERS activity and photothermal properties using a seed-mediated method [34]. Meanwhile, Gao et al. developed TiO_2-coated gold nanosheets (AuNPL@TiO_2) with tunable shell thickness (Figure 1I) [33]. The extinction spectra reveal that thicker TiO_2 shells reduce heat dissipation and enhance optical absorption (Figure 1J). Under 1064 nm laser irradiation, AuNPL@TiO_2-4 exhibits a temperature increase to 66.3 °C, significantly higher than AuNPL@TiO_2-1 (39.3 °C) (Figure 1K). In vivo experiments demonstrate near-complete tumor ablation with combined SDT and PTT, while maintaining stable body weight over 15 days (Figure 1L). These findings indicate that thermal confinement via shell engineering is a key factor in improving photothermal efficiency. More broadly, these results highlight a critical design principle: Optimizing heat retention (via shell thickness or hybrid structures) is as important as maximizing light absorption.

Further advancements include Au nanorods with tunable LSPR under 980 nm irradiation [35] and Au nanoframes with large mesopores (40 nm), synthesized via a liposome-templated method [36]. The latter exhibits a photothermal efficiency of 23.9% under 1064 nm irradiation. Additionally, Au nanoshell–mesoporous silica hybrid systems provide enhanced mechanical and thermal stability [37]. In addition to plasmonic nanostructures, gold nanoclusters (Au NCs) represent an emerging class of NIR-II agents due to their ultrasmall size, excellent biocompatibility, and renal clearance capability [38]. Their strong photostability and ability to form Au–S bonds with thiol-containing molecules (e.g., glutathione, GSH) further expand their functionality (Figure 2A). For example, Yang et al. developed a dual-functional nanomedicine (Au NCs-Pt) for simultaneous imaging and therapy [39]. By depleting intracellular GSH via Au–S interactions, the system enhances the efficacy of Pt-based chemotherapy. Au NCs-Pt exhibits distinct absorption peaks at 945 and 1035 nm (Figure 2B), enabling NIR-II imaging-guided therapy. Tumor growth is significantly suppressed (~680 mm^3 vs. ~4000 mm^3 in PBS group) after 8 days (Figure 2C), while minimizing systemic toxicity compared to free CDDP. Collectively, these findings demonstrate that ultrasmall gold nanoclusters provide a unique advantage in balancing therapeutic efficacy and biosafety, addressing one of the major limitations of larger plasmonic nanostructures. Another such system, $AuCu_9S_5$ nanoparticles further illustrate the importance of plasmonic coupling effects. Ding et al. (2014) developed dual-plasmonic $AuCu_9S_5$ nanoparticles by integrating Au and Cu_9S_5 components [40]. As shown in Figure 2D, strong LSPR coupling arises from the interaction between electron oscillations in Au and hole oscillations in Cu_9S_5. The absorption spectrum exhibits dual peaks at 550 nm and 1100 nm (Figure 2E), covering both visible and NIR regions. Under 1064 nm laser irradiation, $AuCu_9S_5$ nanoparticles exhibit rapid temperature increases (Figure 2F), with a 12.3 °C rise within 300 s at 0.5 W cm^{-2}, indicating efficient photothermal efficiency. Despite these advances, a key limitation of these systems remains their poor biodegradability and long-term accumulation, which may hinder clinical translation. Therefore, future research should focus on developing biodegradable, cost-effective, and scalable synthesis strategies.

Overall, gold-based nanomaterials offer excellent NIR-II photothermal efficiency due to tunable LSPR, high stability, and biocompatibility. Their efficiency is strongly dependent on structural design (shape, size, coatings) and alloying strategies, which enhance light absorption and heat retention. While ultrasmall Au nanoclusters improve biosafety, future work should focus on biodegradability, reduced long-term toxicity, and scalable synthesis to facilitate clinical translation.

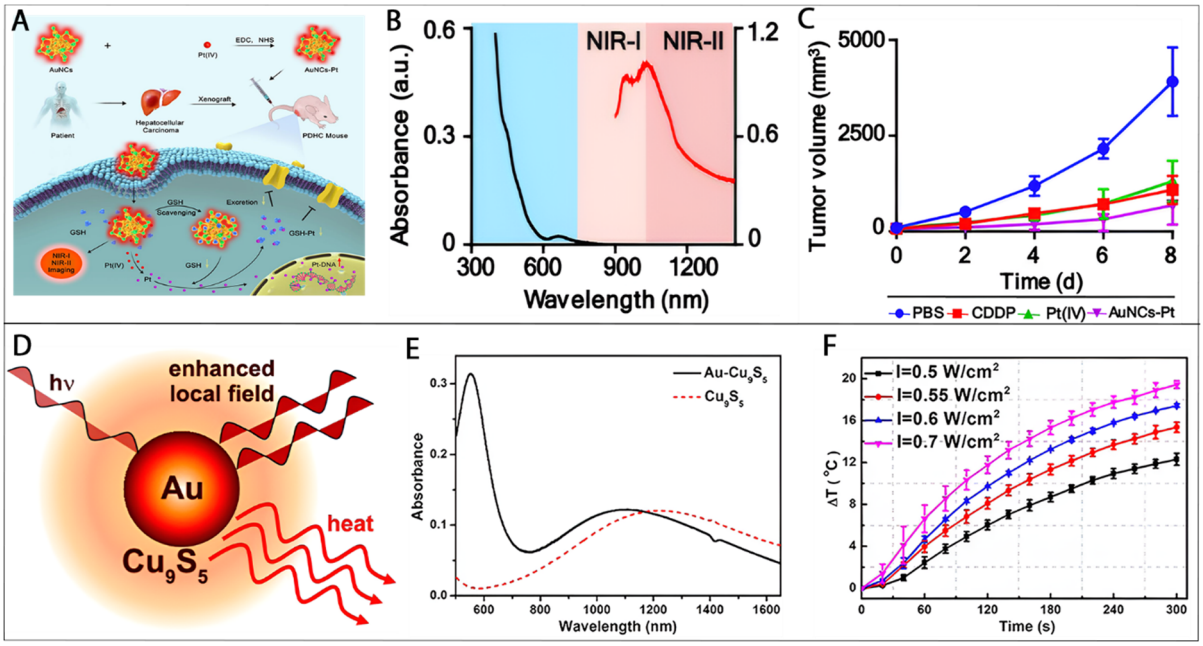

Figure 2. Bioapplication and synthesis of gold-based NIR-II nanomaterials. (**A**) Schematic illustration of Au NCs–Pt for hepatocellular carcinoma treatment via NIR-I/NIR-II imaging and glutathione (GSH) depletion. (**B**) UV–vis absorption and fluorescence spectra of Au NCs–Pt. (**C**) Tumor growth curves following different treatment groups (Reprinted/adapted with permission from Ref. [39]. 2020, American Chemical Society). (**D**) Schematic representation of Au–Cu_9S_5 nanoparticles. (**E**) UV–vis absorption spectra of Au–Cu_9S_5 and Cu_9S_5 nanoparticles. (**F**) Photothermal temperature profiles of Au–Cu_9S_5 nanoparticles (50 ppm) at tumor sites under laser irradiation across different treatment groups (Reprinted/adapted with permission from Ref. [40]. 2014, American Chemical Society).

2.2. Utilization of Metal Alloys for NIR-II Applications

In materials science, the integration of multiple metallic elements into intermetallic compounds or alloyed nanostructures, particularly binary and ternary nanoparticles has emerged as an effective strategy to enhance and tailor physicochemical properties at the nanoscale [41]. The unique appeal of these nanomaterials lies in their tunable structure, atomic distribution, and particle size, all of which significantly influence their optical, electronic, and catalytic behavior. Previous studies have demonstrated that metal alloys exhibit not only enhanced catalytic activity but also improved fluorescence characteristics compared to their monometallic counterparts [10]. Importantly, alloying enables the preservation of key features such as water solubility, biocompatibility, and fluorescence, while simultaneously introducing new functionalities through synergistic interactions between different metal components. For example, Millstone's group incorporated Cu into luminescent Au nanodots to form Au/Cu alloy nanodots, where gradual variation in Cu concentration resulted in a red-shift of the emission spectrum from the NIR-I to the NIR-II windows [42]. Similarly, the incorporation of Co into Au nanodots led to the formation of Au/Co alloy nanodots with tunable NIR fluorescence and additional magnetic properties [43]. Compared to conventional quantum dots, these alloy nanodots offer a distinct advantage by avoiding toxic heavy metals while enabling multifunctionality within a single platform, making them highly attractive for multimodal bioimaging applications. From a design standpoint, these findings highlight that precise compositional tuning in alloy systems directly governs emission wavelength and functionality, providing a powerful approach for engineering NIR-II-active nanomaterials.

Building on this concept, Marbella et al. synthesized Au_xCo_y nanoparticle alloys via the co-reduction of $HAuCl_4$ and $Co(NO_3)_2$ using $NaBH_4$ in the presence of PEGSH ligands [43]. The resulting Au_xCo_y nanoparticles ($y = 26.8 \pm 2.0\%$ Co) exhibit discrete, crystalline, pseudospherical morphologies with core sizes of 2.1–2.3 nm, as shown in Figure 3A–C. The hydrodynamic diameter, determined by pulsed-field gradient stimulated echo (PFGSE) ^1H NMR, ranges from 4.1 to 4.3 nm, reflecting the presence of a PEG shell. A key observation is that Au_xCo_y nanoparticles exhibit photoluminescence (PL) in the NIR region, representing one of the first reports of optical emission from Au–Co alloy systems. Notably, all compositions display optical emission except pure Co nanoparticles. As illustrated in Figure 3D, increasing Co content initially induces a hypsochromic shift (~25 nm) in emission wavelength relative to pure Au nanoparticles, followed by a bathochromic shift at higher Co concentrations (>60%). This behavior correlates with XPS results, indicating increased Co oxidation and lattice expansion at higher Co content. Mechanistically, optical emission in these systems is attributed to Au–thiolate

surface charge-transfer states [44–46]. The incorporation of secondary metals (e.g., Cu or Co) modifies these interactions by altering the local electronic environment, thereby tuning emission properties [47,48]. However, as shown in Figure 3E, the dependence of optical emission on composition is less pronounced in Au_xCo_y systems, suggesting that Co incorporation does not significantly perturb the emissive center. These results reveal an important insight: not all alloying elements contribute equally to optical modulation; the position and electronic role of dopants are critical in determining NIR emission behavior.

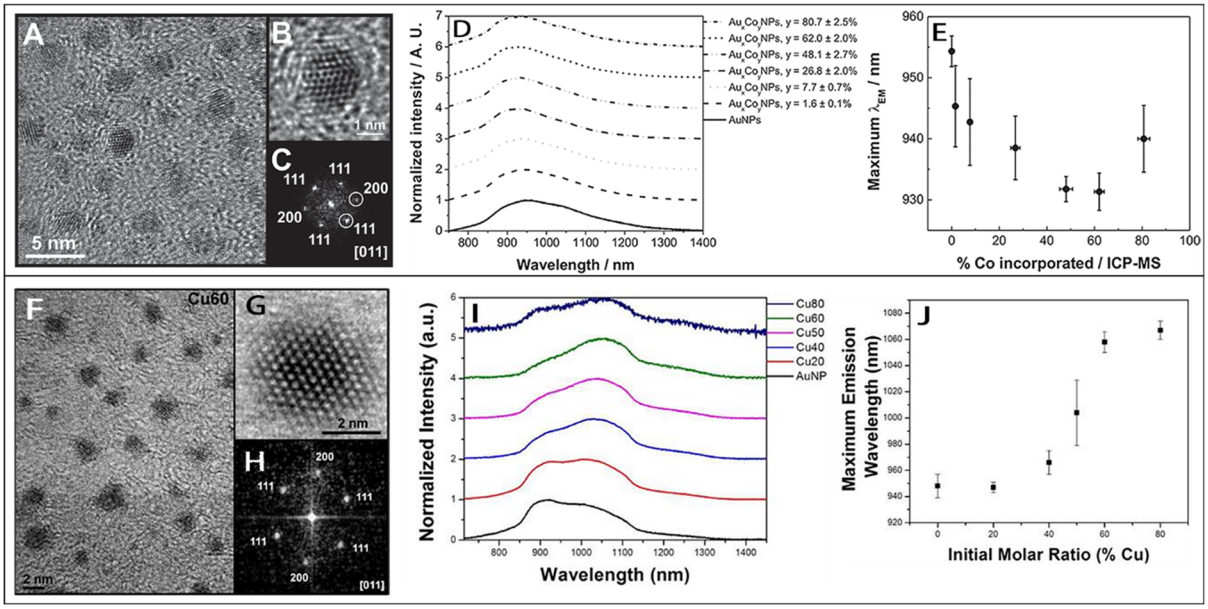

Figure 3. Structural characterization and photoluminescence properties of NIR-II metal alloys. (**A**) HRTEM image of Au_xCo_y nanoparticles. (**B**) Enlarged image of Au_xCo_y nanoparticles and (**C**) the corresponding FFT pattern. (**D**) Photoluminescence emission spectrum of Au_xCo_y nanoparticles in D_2O showing distinct emission behavior. (**E**) Plot of the highest emission wavelength versus Co content (Reprinted/adapted with permission from Ref. [43]. 2014, WILEY-VCH Verlag GmbH & Co. KGaA). (**F**) HRTEM image of Au_xCu_y nanoparticles (Au:Cu = 40:60). (**G**) Enlarged image of Au_xCu_y nanoparticles and (**H**) the corresponding FFT pattern. (**I**) Normalized and offset emission spectra of Au_xCu_y nanoparticles excited at 360 nm. (**J**) Mean emission wavelength as a function of initial Cu molar ratio (Reprinted/adapted with permission from Ref. [42]. 2013, American Chemical Society).

Further advances were reported by Andolina et al., who synthesized ultrasmall Au–Cu metal alloy with tunable Cu molar ratios (0–100%) via co-reduction of $HAuCl_4$ and $Cu(NO_3)_2$ in the presence of PEG-SH ligands [42]. These systems exhibit sizes ranging from 1.9 to 3.0 nm, as confirmed by PFGSE ^{1}H NMR and electron microscopy (Figure 3F–H). The hydrodynamic size is consistently larger than the metallic core, indicating a PEG shell thickness of approximately 1.6–3.2 nm. Structural analysis using fast Fourier transform (FFT) of HRTEM images confirms alloy formation, with lattice parameters deviating from bulk gold due to particle size effects and lattice strain (Figures 3H). Despite these structural variations, a strong correlation between alloy composition and photoluminescence properties is observed. Specifically, increasing Cu content induces a bathochromic shift in optical emission from 947 to 1067 nm (Figure 3I,J), while the full width at half-maximum (FWHM) remains largely unchanged. This behavior suggests that alloy composition primarily influences emission energy levels without significantly affecting emission bandwidth, which is advantageous for maintaining spectral stability in imaging applications. Importantly, no evidence links the observed optical emission to copper complexes or isolated Cu nanoparticles, confirming that emission originates from the alloyed structure itself. Collectively, these studies establish that alloy engineering provides a versatile platform for tuning NIR-II optical properties through controlled compositional variation and electronic coupling.

Unlike single-metal systems, metal alloy nanostructures offer a higher degree of freedom in tuning optical and functional properties. However, their performance is highly dependent on fine control over composition and nanoscale structure, making rational design and reproducibility key factors for future clinical translation.

2.3. Utilization of Metal-Based 2D Nanomaterials for NIR-II Applications

Two-dimensional (2D) nanomaterials have drawn more and more attention in NIR-II applications due to their remarkable physicochemical characteristics, such as their large surface area, ultrathin structure, and efficient

photothermal efficiency under near-infrared windows [49,50]. These characteristics enable enhanced light absorption, rapid heat generation, and high loading capacity for therapeutic agents. Representative examples of metal-based 2D materials for NIR-II applications include MoS_2 [51] and MXene-based systems such as Nb_2C–PVP [52]. A notable example is the work by Lin et al., who developed ultrathin Nb_2C MXene nanosheets (NSs) using a two-step liquid exfoliation strategy involving HF etching and tetrapropylammonium hydroxide (TPAOH) intercalation [52]. As illustrated in Figure 4A, the resulting Nb_2C NSs exhibit excellent dispersibility and functionality in both NIR-I and NIR-II windows. The UV–vis absorption spectra (Figure 4B) show a broad absorption band across these regions, with extinction coefficients of 37.6 L g^{-1} cm^{-1} at 808 nm and 35.4 L g^{-1} cm^{-1} at 1064 nm. Upon laser irradiation, the temperature increase of Nb_2C solutions is strongly dependent on laser power density, indicating efficient photothermal efficiency. In vivo experiments demonstrate that, following intravenous injection of Nb_2C–PVP (20 mg kg^{-1}), tumor-site temperatures rapidly increase from ~30 °C to ~61 °C (808 nm) and ~65 °C (1064 nm) within 10 min (Figure 4C). The corresponding photothermal efficiency are 36.5% and 46.65% upon laser irradiation at 808 nm and 1064 nm, respectively [53]. Tumor growth analysis further reveals complete tumor ablation without recurrence in the NIR-II-treated group (Group 6) over 16 days (Figure 4D), with no significant body weight loss observed. From a mechanistic perspective, the superior performance of Nb_2C MXene can be attributed to its metallic conductivity and high free electron density, which enhance light absorption and nonradiative relaxation processes. Notably, the higher photothermal efficiency observed under NIR-II irradiation suggests that MXene-based materials are particularly well-suited for deeper tissue applications, where reduced scattering and improved penetration are critical. These findings emphasize an important design principle: Electronic structure (metallic vs semiconducting) plays a decisive role in determining NIR-II photothermal efficiency.

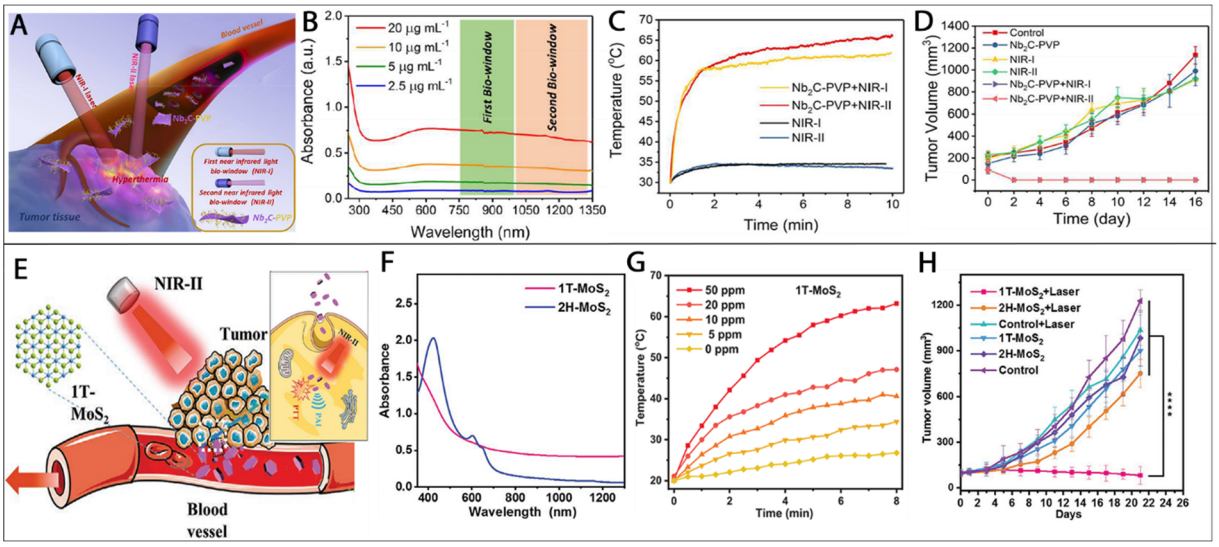

Figure 4. Metal-based two-dimensional (2D) nanomaterials for NIR-II photothermal therapy. (**A**) Schematic representation of PVP-modified 2D biodegradable Nb_2C for in vivo photothermal tumor ablation in NIR-I and NIR-II bio-windows. (**B**) UV–vis absorption spectra of Nb_2C nanosheets at different concentrations. (**C**) Temperature change curves of different groups at tumor sites under laser irradiation. (**D**) Tumor growth curves after different treatment groups (Reprinted/adapted with permission from Ref. [52]. 2017, American Chemical Society). (**E**) Schematic representation of 1T-MoS_2 nanodots as a PAI-guided PTT agent. (**F**) UV–vis absorption spectra of 1T-MoS_2 and 2H-MoS_2 nanodots. (**G**) Temperature change curves of PVP-modified 1T-MoS_2 at tumor sites under laser irradiation. (**H**) Tumor growth curves after different treatment groups (Reprinted/adapted with permission from Ref. [54]. 2020, Wiley-VCH GmbH).

Further insights into structure–property relationships are provided by Zhou et al. (2020), who synthesized single-layer metallic 1T-phase MoS_2 (1T-MoS_2) nanodots from bulk 2H-phase MoS_2 via lithium intercalation [54]. As shown in Figure 4E, this phase transition enables the exploration of phase-dependent performance for photoacoustic imaging (PAI)-guided PTT. Unlike semiconducting 2H-MoS_2, the metallic 1T-MoS_2 exhibits a broad and featureless absorption spectrum extending from the visible to the NIR windows (Figure 4F), which is highly advantageous for PTT. The heating curves (Figure 4G) demonstrate that PVP-modified 1T-MoS_2 nanodots can increase the temperature by 43.0 °C within 8 min, even at low concentrations (50 ppm), whereas pure water shows only a 6.8 °C increase under identical conditions. In contrast, 2H-MoS_2 nanodots exhibit a significantly lower temperature increase of 12.4 °C. This direct comparison clearly indicates that phase engineering (1T vs 2H)

plays a critical role in determining photothermal efficiency. The metallic 1T phase facilitates enhanced electron mobility and nonradiative energy dissipation, leading to superior heat generation efficiency. Additionally, the temperature rise is positively correlated with nanodot concentration, further confirming their tunable photothermal performance. In vivo studies (Figure 4H) confirm that 1T-MoS_2 nanodots enable effective tumor ablation with minimal systemic toxicity, demonstrating their potential as safe and efficient NIR-II photothermal agents.

Compared to conventional nanostructures, metal-based 2D nanomaterials offer distinct advantages in NIR-II PTT due to their tunable electronic structure and large surface area. However, their performance is highly dependent on phase control, surface engineering, and structural stability, which must be carefully optimized for successful clinical translation.

3. Hybrid and Composite NIR-II Nanomaterials

Hybrid and composite NIR-II nanomaterials integrate multiple functional components into a single platform to enhance optical performance, structural stability, and therapeutic efficacy. By combining different materials, these systems can overcome the intrinsic limitations of single-component nanostructures, such as insufficient absorption, poor stability, or lack of multifunctionality. A representative example is ammonium tungsten bronze ($(NH_4)_xWO_3$), which exhibits a high attenuation coefficient, broad light absorption, and low cost, making it a promising candidate for NIR-II PTT. Cheng et al. (2019) further improved its performance by developing 2D ultrathin tellurium oxide/$(NH_4)_xWO_3$ nanoribbons (TeO_2/$(NH_4)_xWO_3$, TONW NRs) [55]. These nanoribbons exhibit significantly enhanced near-infrared absorption due to LSPR arising from free electrons. Compared to pure ammonium tungsten bronze nanoparticles, TONW NRs show markedly improved NIR-II absorption, which is attributed to electronic interactions between W^{6+} centers and Te atoms, leading to enhanced charge redistribution. To improve dispersibility and biocompatibility, PEGylated TONW nanoribbons (PEG-TONW NRs) were prepared by coating with DSPE-PEG (Figure 5A). Their absorption spectra confirm strong photothermal performance, with temperature increases upon laser irradiation at 1064 nm proportional to nanomaterials concentration (Figure 5B,C). These results demonstrate that heterostructure engineering (TeO_2 integration) can effectively amplify NIR-II absorption and photothermal efficiency. From a design perspective, this system highlights that: interfacial electronic coupling in hybrid nanostructures is a key factor in enhancing NIR-II photothermal efficiency.

Beyond inorganic hybrids, organic–inorganic composite systems have also shown significant promise. Yang et al. constructed a multifunctional nanocarrier composed of biodegradable charged polyester vectors (BCPVs) and graphene quantum dots (GQDs) for pancreatic cancer therapy [56]. This system enables co-delivery of doxorubicin (DOX) and small interfering RNA (siRNA), while GQDs provide photothermal functionality. Upon laser irradiation, the GQD/DOX/BCPV/siRNA nanostructure facilitates controlled drug release alongside simultaneous PTT. Similarly, Cui et al. (2021) developed reduced graphene oxide (rGO) coated with lipid bilayers and functionalized with mesoporous silica nanosheets, serving as both a photothermal agent and an NIR-triggered drug delivery platform [57]. Compared to single-component graphene systems, these composites exhibit improved stability, drug loading capacity, and controlled release behavior. These studies collectively indicate that: Hybridization with polymers, lipids, or mesoporous structures significantly enhances drug delivery capability and therapeutic synergy in NIR-II nanostructures.

In addition to these systems, carbon-based hybrid nanomaterials have demonstrated excellent photothermal performance. Xu et al. developed hollow carbon nanospheres functionalized with polyethylene glycol-graft-polyethylenimine (HPP) [58]. The HPP system exhibits high biocompatibility, a stable core–shell structure, and an impressive photothermal efficiency of 45.1% under NIR-II laser irradiation. The synthesis process of HPP is illustrated in Figure 5D. Monodispersed SiO_2 nanoparticles (~180 nm) were first prepared using tetraethyl orthosilicate (TEOS) with ethylenediamine (EDA) as a catalyst. A resorcinol–formaldehyde polymer layer was then coated as a hard template. After carbonization and etching, hollow carbon nanospheres were obtained, forming the HPP structure with a large internal cavity. Upon laser irradiation at 1064 nm, the temperature of HPP aqueous dispersions increased significantly with concentration, ranging from 17 °C to 44 °C within approximately 7 min (Figure 5E), whereas pure water showed only minimal heating (~8 °C). In vivo studies (Figure 5F) demonstrate that the HPP + laser group exhibits complete suppression of tumor growth, while control groups show significant tumor progression. Importantly, no noticeable body weight loss was observed, indicating good biocompatibility and safety. The superior performance of HPP can be attributed to its hollow structure and high surface area, which enhance light absorption, heat generation, and drug-loading capacity. This highlights another important design principle: Structural engineering (e.g., hollow architectures) can significantly improve both photothermal efficiency and drug delivery functionality.

Overall, hybrid and composite NIR-II nanomaterials offer a powerful strategy to overcome the limitations of single-component systems by integrating multiple functionalities into a unified platform. However, their clinical translation depends on achieving a balance between functional complexity and synthetic simplicity, as well as ensuring reproducibility, safety, and scalability.

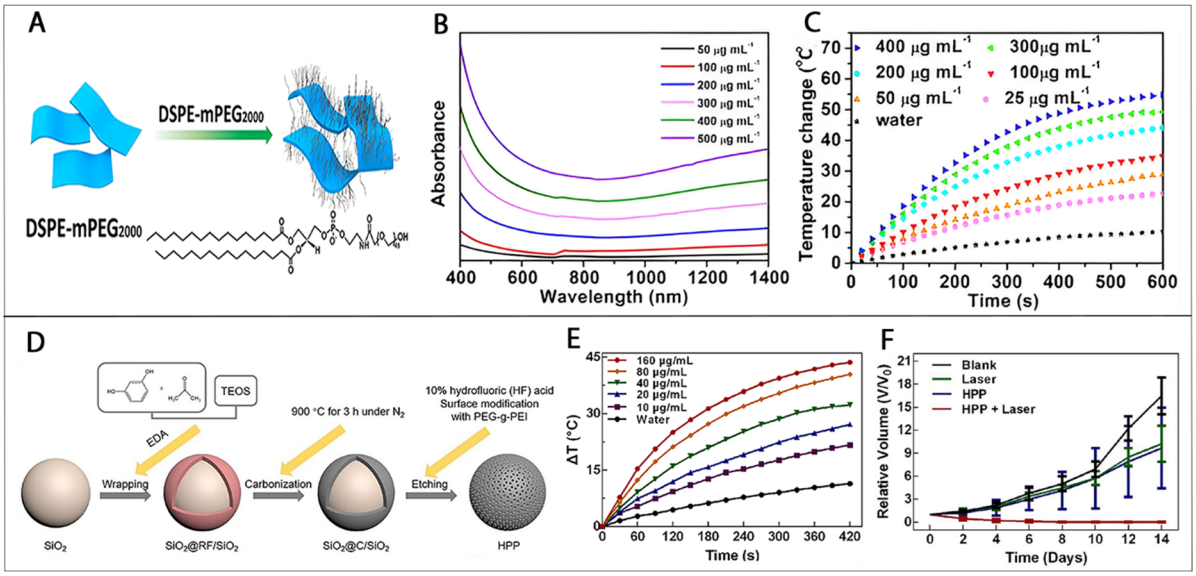

Figure 5. Hybrid and composite-based NIR-II nanomaterials in photothermal therapy. (**A**) Synthesis process of PEG-TONW nanorods. (**B**) UV–vis absorption spectra of PEG-TONW nanorods at different concentrations. (**C**) Temperature change curves of PEG-TONW nanorods at tumor sites under 1064 nm laser irradiation in different treatment groups (1.0 W cm^{-2}) (Reprinted/adapted with permission from Ref. [55]. 2019, American Chemical Society). (**D**) Schematic representation of the HPP synthesis process. (**E**) Temperature change curves of HPP at tumor sites under 1064 nm laser irradiation in different treatment groups. (**F**) Tumor growth curves after different treatment groups (Reprinted/adapted with permission from Ref. [58]. 2021, Springer Nature).

4. Semiconductor and Carbon-Based NIR-II Fluorophores

Semiconductor and carbon-based NIR-II fluorophores have emerged as important alternatives to metal-based systems due to their tunable optical properties, reduced toxicity, and excellent imaging performance. Unlike plasmonic materials that primarily rely on photothermal effects, these fluorophores enable high-resolution fluorescence imaging with deeper tissue penetration, making them particularly suitable for diagnostic and image-guided therapeutic applications. In addition to their optical advantages, recent studies have highlighted the importance of nanoparticle stability and storage for practical biomedical applications. For example, lyophilized 'off-the-shelf' nanoparticle formulations have demonstrated the ability to maintain physicochemical properties and biological functionality during long-term storage at ambient conditions, providing a promising strategy to enhance the scalability and clinical translation of NIR-II nanostructures [59].

4.1. Utilization of Carbon-Based Nanomaterials for NIR-II Applications

In recent years, like other carbon-based nanomaterials, single-walled carbon nanotubes (SWCNTs) exhibit unique optical properties arising from their bandgap-dependent electronic structure. Upon photon excitation, SWCNTs absorb light in the visible (400–700 nm) and NIR-I (650–950 nm) regions and emit fluorescence in the NIR-II windows. This large Stokes shift minimizes reabsorption and enables efficient deep-tissue imaging without significant thermal loss [60]. In addition, SWCNTs possess diameters of approximately 1 nm and lengths ranging from 100 to 1000 nm, and can be dispersed in aqueous environments using suitable surfactants or biomolecular coatings. Their broad absorption spectrum, excellent photostability, and intrinsic NIR-II fluorescence make them highly suitable for optical biosensing, fluorescence labelling, and in vivo imaging [61–63]. Consequently, SWCNTs have been widely applied in FLI, PTT, PDT, and deep-tissue imaging applications [61,64–67]. A key advantage of SWCNTs lies in their versatile surface functionalization. Coating with surfactants, polymers, DNA, proteins, or viruses enables targeted delivery and enhanced biological compatibility [68]. For example, Belcher's group functionalized SWCNTs using the M13 bacteriophage to create SBP-M13-SWNT, a targeted NIR-II imaging agent (Figure 6A) [69]. This system incorporates three components: the SPARC-binding peptide (SBP),

the M13 virus scaffold, and SWCNTs. Since SPARC is overexpressed in advanced ovarian cancer and associated with poor prognosis [70], this targeting strategy enables selective tumor imaging. Optical characterization (Figure 6B) confirms that SBP-M13-SWNTs retain fluorescence properties comparable to unmodified SWCNTs, while avoiding aggregation-induced quenching. In vivo studies demonstrate that this system enables non-invasive tumor detection and improves surgical precision. Specifically, image-guided surgery increased tumor removal depth from 1.3 mm to 3 mm, particularly for small tumors. Repeated imaging-guided procedures further reduced tumor burden (Figure 6C,D). These findings highlight an important principle: Biological functionalization (e.g., virus-assisted targeting) can significantly enhance the clinical utility of NIR-II fluorophores beyond intrinsic optical properties.

Further advancements were reported by Hong et al., who developed SWCNT-IRDye800 nanostructures for in vivo cerebrovascular imaging [65]. Using NIR-II fluorescence imaging, signals were detected up to 2.6 mm deep within the mouse skull, enabling high-resolution visualization of brain vasculature. Comparative analysis across spectral windows (NIR-I, NIR-II, and NIR-II a) revealed that the NIR-II a region (1.3–1.4 µm) provides superior image clarity and signal-to-noise ratio due to reduced photon scattering (Figure 6E). High-resolution imaging of cerebral vessels, including the sagittal sinus and transverse sinus, was achieved (Figure 6E), with further enhancement using microscopic objectives (Figure 6F). The use of large-diameter SWCNTs enabled emission in the optimal NIR-II a window (Figure 6G), improving imaging depth and resolution. These findings demonstrate that emission wavelength engineering within the NIR-II sub windows is critical for optimizing imaging performance.

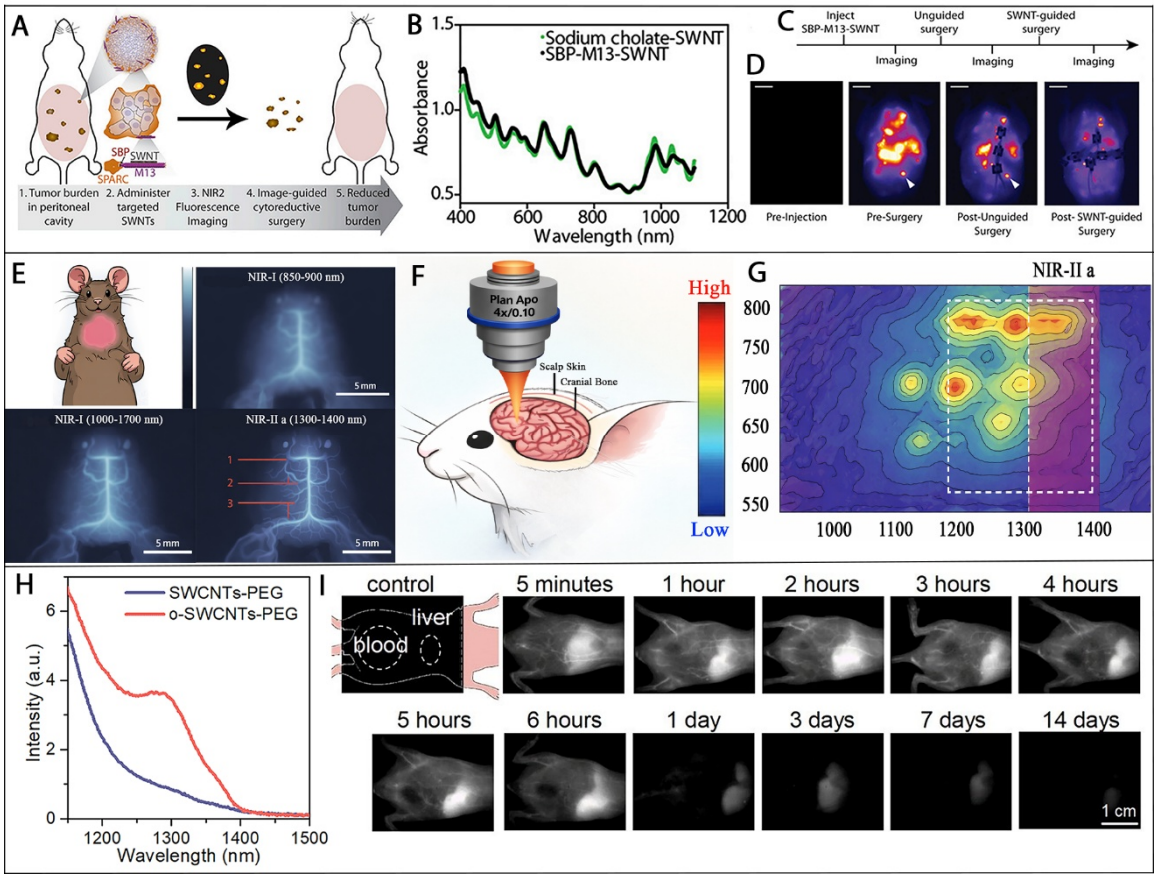

Figure 6. Single-walled carbon nanotube (SWCNT)-based NIR-II nanoprobes for deep-tissue imaging and surgical guidance. (**A**) Schematic illustration of the relationship between ovarian tumor nodules and NIR-II fluorescence for non-invasive tumor identification and surgical excision. (**B**) UV–vis absorption spectra of SWNTs in sodium cholate and SBP-M13-SWNT agent. (**C**) Schematic illustration of serial surgical procedures. (**D**) Whole-abdomen NIR-II images acquired before SBP-M13-SWNT injection, before surgery, after the first unguided surgery, and after the second SWNT-guided SBP-M13 procedure; white arrows indicate nodules identified only during image-guided surgery and SWNT-positive sites (Reprinted/adapted with permission from Ref. [69]. 2014, Proceedings of the National Academy of Sciences). (**E**) NIR-I, NIR-II, and NIR-IIa fluorescence images of mouse skull and brain using SWNT-IRDye800; visualization of transverse sinus, superior sagittal sinus, and inferior cerebral vein (1, 2, and 3, respectively) in a hairless C57BL/6 mouse. (**F**) Schematic illustration of NIR-IIa fluorescence penetration through scalp, skull, and brain tissue. (**G**) Photoluminescence excitation spectrum of LS nanotubes in aqueous solution; red

region indicates the 1.3–1.4 μm NIR-IIa window. (**H**) UV–vis absorption spectra of SWCNT-PEG (blue) and o-SWCNT-PEG (red) in aqueous solution. (**I**) In vivo imaging of mice at a specified time point after injection of 30 μg o-SWCNT-PEG (Reprinted/adapted with permission from Ref. [62]. 2019, American Chemical Society).

In addition, Okazaki et al. developed oxygen-modified SWCNTs (o-SWCNT-PEG) by introducing epoxide groups, enabling optical emission at 1300 nm under 980 nm laser irradiation [62,71]. Unlike pristine SWCNTs, which lack emission at this excitation wavelength, the modified nanotubes exhibit strong fluorescence due to altered electronic states (Figure 6H). In vivo studies show stable fluorescence intensity over 6 h, with gradual clearance over 14 days (Figure 6I), consistent with previous reports on long-term biodistribution [72]. Collectively, these studies demonstrate that chemical modification of SWCNTs is an effective strategy to tailor emission properties and improve imaging performance, although issues related to long-term retention and low quantum yield (<1%) remain. Such improved optical characteristics have enabled their practical application in bioimaging; for instance, Welsher et al. employed SWCNTs as primary NIR-II fluorescence agents to achieve superior temporal–spatial resolution and deeper tissue penetration in fluorescence imaging [73].

Beyond SWCNTs, other carbon-based nanomaterials have been developed for NIR-II photothermal applications, including N-doped carbon dots (CDs), carbon fibers, carbon nano-onions, and carbon-based nanocomposites such as carbon–silica nanostructures [74–82]. These nanomaterials exhibit strong photothermal efficiency and flexible functionalization capabilities. A representative example is the hybrid NIR-II-CD/BP system developed by Geng et al. (2019), which combines black phosphorus nanosheets (BP NSs) with NIR-II carbon dots (Figure 7A) [51]. The hybrid structure enhances NIR absorption due to increased free carrier concentration and plasmonic effects (Figure 7B) [40,83]. Notably, the absorption intensity at 1064 nm (0.590) exceeds the sum of individual components (0.425), indicating synergistic interaction rather than simple physical mixing. Under 1064 nm laser irradiation, the NIR-II-CD/BP system exhibits a temperature increase of 25.7 °C, outperforming NIR-II-CDs (20.2 °C) and BP alone (16.3 °C) (Figure 7C). The photothermal efficiency reaches 61.4%, significantly higher than that of pristine BP (28.4%). In vivo results demonstrate complete tumor elimination without recurrence in the treated group (Figure 7D), with no observable toxicity. This clearly demonstrates that hybridization with carbon dots can enhance both stability and photothermal efficiency of otherwise unstable materials.

Further optimization was achieved through N-doped graphitic carbon dots with a high photothermal efficiency of 81.3% [74]. These nanomaterials rapidly increase tumor temperature under 1064 nm laser irradiation and can also function as drug carriers. To enable multifunctional therapy, PEGylated thermosensitive liposomes (TSLs) were developed to encapsulate NIR-II-CDs and ICG, along with DOX for combined photothermal–chemotherapy (Figure 7E). Upon 1064 nm laser irradiation, tumor temperature rapidly increases (Figure 7F), resulting in effective tumor ablation (Figure 7G). Notably, complete tumor eradication without recurrence is achieved in the NIR-II-CD/ICG/DOX/TSL group, whereas free DOX shows negligible therapeutic effect. These findings emphasize a key insight: integration of imaging agents, photothermal materials, and chemotherapeutics into a single nanoplatform enables highly effective synergistic therapy in the NIR-II windows.

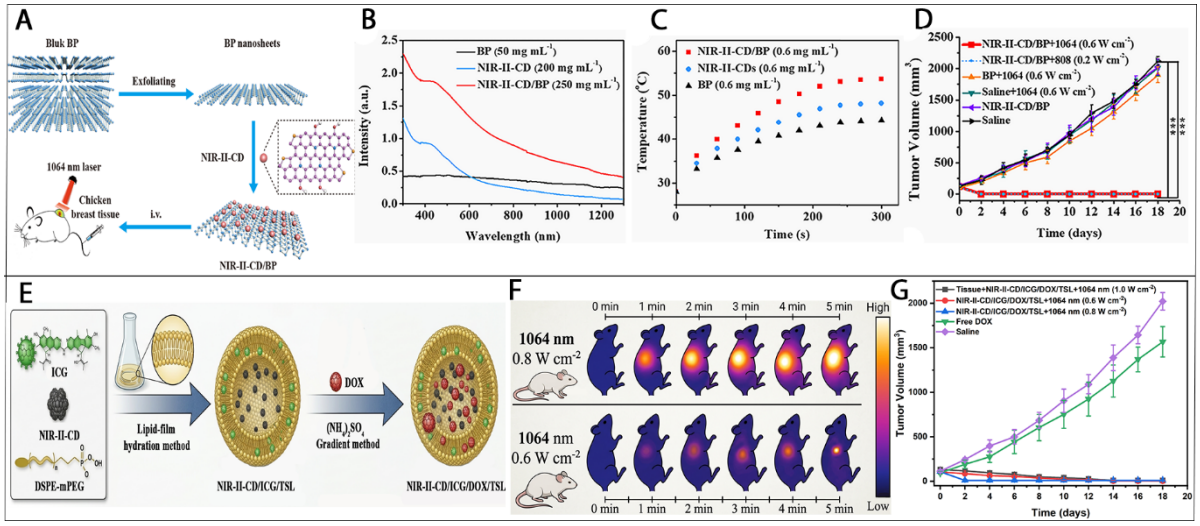

Figure 7. Carbon-based nanomaterials for NIR-II photothermal therapy and synergistic cancer treatment. (**A**) Schematic representation of the synthesis procedure of NIR-II-CD/BP. (**B**) UV–vis absorption spectra of BP nanosheets, NIR-II-CD, and NIR-II-CD/BP at different concentrations. (**C**) Temperature change curves at tumor sites under 1064 nm laser irradiation in different treatment groups. (**D**) Tumor growth curves after different treatment group

(Reprinted/adapted with permission from Ref. [51]. 2019, American Chemical Society). (**D**) Schematic representation of the synthesis process of NIR-II-CD/ICG/DOX/TSL (TSL: PEG-coated Thermosensitive Liposome). (**E**) Schematic representation of the synthesis process of NIR-II-CD/ICG/DOX/TSL (TSL: PEG-coated thermosensitive liposome). (**F**) Infrared thermographic images of NIR-II-CD/ICG/DOX/TSL solutions in centrifuge tubes under 1064 nm laser irradiation at 0.8 and 0.6 W cm^{-2}. (**G**) Tumor growth curves after different treatment groups.

Overall, carbon-based NIR-II fluorophores offer a unique combination of optical tunability, photostability, and multifunctionality. However, their clinical translation depends on overcoming challenges related to low quantum efficiency, long-term biosafety, and reproducibility, while leveraging hybrid and multifunctional strategies to maximize therapeutic and diagnostic performance.

4.2. Utilization of Semiconductor Quantum Dots for NIR-II Applications

Expanding the scope of NIR-II fluorescent nanomaterials, semiconductor quantum dots (QDs), including GQDs and metal chalcogenide QDs such as Ag_2S, have attracted significant attention due to their strong NIR fluorescence, tunable optical emission, and relatively low biological toxicity. Their emission can be adjusted over a broad spectral range (687–1294 nm), enabling applications across both NIR-I and NIR-II imaging windows.

Compared with traditional QDs containing toxic heavy metals (e.g., Cd, Pb, Se, Te, As), Ag_2S QDs offer a safer alternative while maintaining excellent optical performance [84,85]. These QDs exhibit small particle sizes (1.6–6.8 nm), high fluorescence stability, strong resistance to photobleaching, and relatively high quantum yields, enabling high spatial and temporal resolution imaging. Furthermore, their size and shape can be precisely controlled to tailor pharmacokinetics and tissue distribution [86]. A landmark study by Wang and Dai demonstrated the use of PEG-modified Ag_2S QDs emitting at 1200 nm for in vivo NIR-II imaging [87,88]. Surface PEGylation significantly improves water solubility and biocompatibility, enabling efficient systemic circulation. Following intravenous injection into tumor-bearing mice, Ag_2S QDs gradually accumulate at tumor sites due to the enhanced permeability and retention (EPR) effect, enabling non-invasive tumor imaging. Importantly, long-term toxicity studies indicate that Ag_2S QDs predominantly accumulate in the reticuloendothelial system (RES), including the liver and spleen, but can be gradually cleared over time without significant adverse effects [89]. These findings suggest that Ag_2S QDs provide a favorable balance between imaging performance and biosafety, addressing a major limitation of conventional QDs. To further enhance imaging performance, Hong et al. developed 6PEG-Ag_2S QDs through surface functionalization with dihydrolipoic acid (DHLA) and PEG ligands, resulting in highly water-soluble nanostructures with an average diameter of ~5.4 nm (Figure 8A) [90,91]. Time-dependent imaging studies (Figure 8B) demonstrate efficient systemic distribution and tumor accumulation. The tumor-to-background ratio (TBR) increases progressively from 30 min to 24 h post-injection, surpassing the Rose threshold after 4 h (Figure 8C), confirming reliable tumor detection [92,93]. These results highlight a key design insight: Surface engineering (e.g., PEGylation) is essential for optimizing biodistribution, circulation time, and imaging contrast in QD-based systems.

Beyond imaging, multifunctional QDs have been developed for combined therapeutic applications. Guo et al. designed $Cu_2(OH)PO_4$@PAA QDs as a "three-in-one" nanoplatform integrating photoacoustic imaging, PTT, and PDT [94]. Under 1064 nm laser irradiation, these QDs exhibit concentration-dependent temperature increases (Figure 8D), demonstrating effective photothermal efficiency. In addition, strong intracellular reactive oxygen species (ROS) generation is observed under NIR laser irradiation (Figure 8E), confirming their PDT capability. Notably, significant ROS production occurs only in the combined QD + laser group, indicating that therapeutic activation is highly controllable. In vivo results (Figure 8F) show near-complete tumor ablation within in most treated animals, with no significant body weight loss. This multifunctional behavior demonstrates that: Integration of PTT and PDT within a single QD platform enables synergistic therapeutic effects and improved treatment outcomes. Further developments include GQDs with enhanced NIR-II absorption. Liu et al. synthesized 9T-GQDs via a one-step solvothermal method, achieving strong absorption around ~1070 nm [95]. As shown is Figure 8G, 9T-GQDs are employed as photothermal agents to kill tumor cells in vitro and prevent tumor development in vivo. Under NIR-II laser irradiation, these nanomaterials exhibit efficient photothermal performance, with temperature increases proportional to concentration (Figure 8H), while control samples show negligible heating. In vivo studies (Figure 8I) demonstrate that tumors in control groups grow rapidly, whereas the 9T-GQDs + NIR-II group exhibits significant tumor suppression. Importantly, no noticeable body weight changes are observed, indicating good biocompatibility.

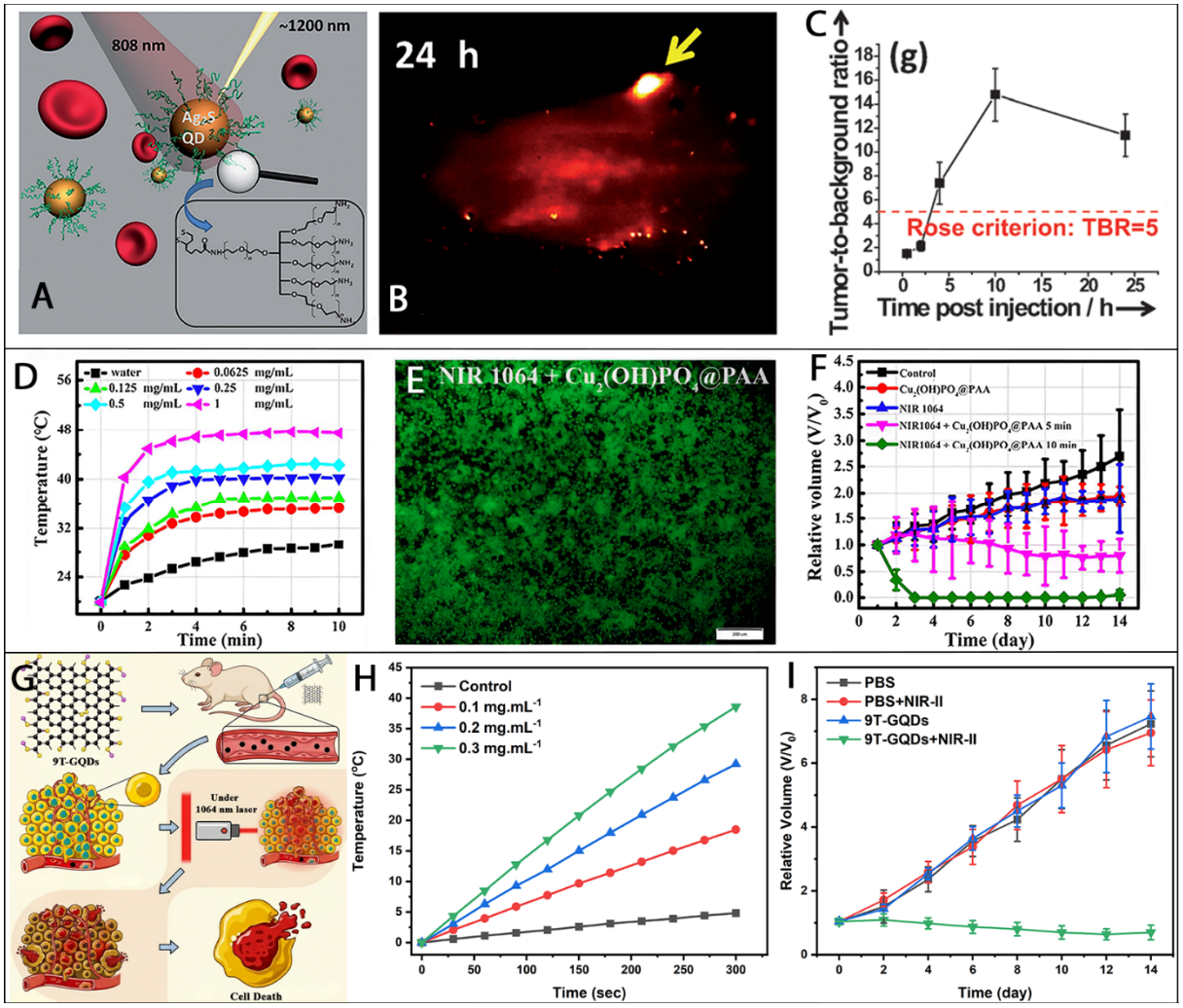

Figure 8. Semiconductor quantum dots for NIR-II imaging and multimodal cancer theranostics. (**A**) Schematic representation of 6PEG-Ag_2S QDs excited at 808 nm and emitting at 1200 nm; PEG coating is shown in the inset. (**B**) Time-lapse NIR-II fluorescence imaging of mice after injection of 6PEG-Ag_2S QDs. (**C**) Tumor detection probability based on the Rose criterion, showing tumor-to-background ratio (TBR) as a function of post-injection time; 100% detection is achieved at 4 h post-injection (Reprinted/adapted with permission from Ref. [87]. 2012, WILEY-VCH Verlag GmbH & Co. KGaA). (**D**) Temperature change curves of $Cu_2(OH)PO_4$@PAA at tumor sites under 1064 nm laser irradiation in different treatment groups (2.0 W cm^{-2}). (**E**) Fluorescence images showing ROS generation in HeLa cells under different irradiation wavelengths. (**F**) Tumor growth curves after different treatment groups (Reprinted/adapted with permission from Ref. [94]. 2017, American Chemical Society). (**G**) Schematic illustration of imaging-guided PTT using 9T-GQDs under NIR-II laser irradiation. (**H**) Temperature change curves of 9T-GQDs at tumor sites under 1064 nm laser irradiation in different treatment groups (1.0 W cm^{-2}). (**I**) Tumor growth curves over 14 days following different treatments.

Collectively, semiconductor quantum dots represent a highly promising class of NIR-II imaging agents due to their tunable optical properties, strong fluorescence, and multifunctional potential. However, their successful clinical translation requires balancing optical performance, biosafety, and clearance behavior, while leveraging surface and structural engineering to optimize imaging and therapeutic outcomes.

5. Organic NIR-II Fluorophores

Organic NIR-II fluorophores have emerged as an important class of imaging agents due to their well-defined molecular structures, excellent biocompatibility, and favorable metabolic profiles. Compared with inorganic nanomaterials, organic fluorophores typically exhibit lower toxicity, improved biodegradability, and more predictable pharmacokinetics, making them highly attractive for clinical translation in cancer theranostics. In general, most fluorescent agents tend to accumulate in the liver and spleen and are gradually cleared from the body [96]. However, compared to inorganic nanostructures, organic fluorophores often demonstrate more efficient

metabolic clearance, which is a critical advantage for reducing long-term toxicity. From a design perspective, the optical properties of organic NIR-II fluorophores are primarily governed by molecular engineering strategies, such as conjugation length extension, donor–acceptor (D–A) interactions, and heteroatom substitution. These approaches enable precise tuning of bandgap, absorption, and emission properties, which is more challenging to achieve in inorganic systems.

5.1. Utilization of Conjugated Polymers for NIR-II Applications

Conjugated polymers have emerged as a powerful platform for NIR-II fluorophores design due to their tunable electronic structures and flexible molecular architectures. In particular, donor–acceptor (D–A) copolymerization is widely employed to reduce the bandgap, thereby shifting absorption and optical emission into the NIR-II windows. The interaction between electron-rich donor units and electron-deficient acceptor units facilitates intramolecular charge transfer, which is critical for achieving long-wavelength optical responses. Semiconducting polymer dots (Pdots), a class of organic fluorescent nanomaterials, exhibit several advantageous properties, including large Stokes shifts, narrow emission bands, high brightness, excellent photostability, and broad absorption spectra. These features make them superior to many traditional fluorescent dyes for applications in molecular detection, bioimaging, and drug delivery [3]. Importantly, conjugated polymers also demonstrate promising photothermal properties in the NIR-II windows. Representative examples include CS-RuO_2NPs [97], P1RGD NPs [98], SPN [13], IR-SS [96], NPPBTPBF-BT [99], and SPNI-I [100], which exhibit high photothermal efficiency and stability. Cao et al. developed a D–A conjugated polymer stabilized with quinoline to extend π-conjugation length, thereby reducing the bandgap and enhancing NIR-II absorption [101]. Specifically, the polymer TBDOPV-DT, synthesized using 2,2′-bithiophene (donor) and p-phenylene vinylene (acceptor), demonstrates efficient NIR-II light absorption and photothermal efficiency. Similarly, Guo et al. (2018) synthesized D–A structured polymer nanoparticles functionalized with C-RGD (Cyclo(Arg-Gly-Asp-D-Phe-Lys (MPA)) targeting ligands, achieving strong NIR-II absorption and effective photothermal performance [98]. Wen et al. further demonstrated that semiconducting polymer nanoparticles (SPNs) with optimized donor–acceptor combinations exhibit enhanced NIR-II optical responses [13]. In addition, Sun et al. employed a terpolymer strategy incorporating one acceptor and two donor units, enabling fine-tuning of optical properties through monomer ratio adjustment [15]. A notable example is the work by Li et al., who developed IR-SS nanoparticles with absorption peaks extending beyond 1000 nm (Figure 9A) [96]. By incorporating benzo[1,2-c:4,5-c′] bis ([1,2,5] thiadiazole) (BBT) as a strong electron acceptor and modifying sulfur atoms with selenium (Se), the authors achieved tunable absorption peaks for IR-TT, IR-SS, and IR-TS at 830 nm, 1120 nm, and 975 nm, respectively (Figure 9B). Under 1064 nm laser irradiation (1 W cm^{-2}), all nanoparticle solutions (100 μg mL^{-1}) exhibit significant temperature increases within 5 min, reaching 47.8 °C (IR-TT), 69.1 °C (IR-SS), and 64 °C (IR-TS) (Figure 9C). In vivo results demonstrate that tumors in control groups (PBS, laser-only, NP-only) grow rapidly, whereas the NP + laser group shows nearly complete tumor inhibition without recurrence over 14 days (Figure 9D). These results highlight that: Heteroatom substitution (e.g., S → Se) and acceptor strength are key parameters for tuning NIR-II absorption and photothermal efficiency.

In addition to molecular design, nanoscale aggregation behavior also plays a critical role. Recently, Pdots have been further optimized by reducing nonradiative decay pathways. Zhang et al. enhanced NIR-II fluorescence by introducing phenothiazine groups to induce aggregation-induced emission (AIE), thereby suppressing energy loss through π–π stacking interactions. Furthermore, the incorporation of bulky side chains reduces interchain interactions, leading to increased fluorescence quantum yield. This dual strategy demonstrates that: Controlling molecular packing and aggregation is essential for maximizing fluorescence efficiency in conjugated polymer systems.

Altogether, organic NIR-II fluorophores offer significant advantages in terms of biocompatibility, biodegradability, and molecular tunability. Unlike inorganic systems, their optical properties can be precisely engineered at the molecular level. However, achieving optimal performance requires careful control over electronic structure, molecular packing, and nanoscale assembly, highlighting the importance of rational molecular design for future clinical applications.

5.2. Donor–Acceptor–Donor (D–A–D) Small-Molecule Fluorophores for NIR-II Applications

Donor–acceptor–donor (D–A–D) small-molecule fluorophores, particularly those based on BBTD (benzobisthiadiazole) derivatives and cyanine dyes, represent one of the most important classes of organic NIR-II imaging agents. These systems are characterized by well-defined molecular structures, tunable electronic properties, and relatively rapid biological clearance, making them highly attractive for clinical translational. From a mechanistic perspective, the D–A–D architecture enables efficient intramolecular charge transfer (ICT) between electron-

donating and electron-accepting units. The spatial arrangement of strong donor groups flanking a central acceptor reduces the HOMO–LUMO energy gap, thereby shifting fluorescence emission toward the NIR-II windows [102]. Importantly, both donor strength and acceptor electron-withdrawing capability can be systematically tuned to precisely control optical properties. A landmark example is CH1055, one of the earliest D–A–D NIR-II fluorophores used for in vivo imaging, which demonstrated rapid pharmacokinetics with approximately 90% renal clearance within 24 h [103]. This highlights a key advantage of small-molecule dyes over many nanomaterial systems: efficient clearance and reduced long-term toxicity. However, conventional BBTD-based fluorophores typically exhibit excitation and emission wavelengths within the 800–1000 nm range, which limits imaging depth. To address this limitation, molecular engineering strategies such as heteroatom substitution and donor strengthening have been explored to further redshift emission into the deeper NIR-II windows. For instance, Fang et al. developed a novel fluorophore, FM1210, by introducing both an amino group and selenium (Se) into the BBTD backbone (Figure 9E) [104]. This modification results in a significant redshift, achieving a maximum emission peak at 1210 nm. The absorption peak of FM1210 in CH_2Cl_2 appears at 980 nm (Figure 9F), enabling deeper tissue penetration and reduced photon scattering. In vivo imaging (Figure 9G) demonstrates that FM1210-NPs accumulate in tumors with a peak tumor-to-background ratio of 2.3 at 4 h post-injection, followed by gradual clearance, reflecting favorable dynamic behavior. These results illustrate a key design principle: Heteroatom engineering (e.g., S → Se) and donor modification are highly effective strategies for extending emission wavelength and improving imaging depth. In parallel, cyanine dyes, which are based on polymethine chain structures, provide an alternative approach for NIR-II fluorophore design. Their optical properties can be tuned by extending the conjugated polymethine chain, modifying heterocyclic donor groups, or replacing heteroatoms (e.g., oxygen with sulfur), all of which contribute to redshifted absorption and emission [105,106]. Cyanine dyes are particularly attractive due to their simple synthesis and strong NIR absorption. Despite these advantages, cyanine-based NIR-II fluorophores face several intrinsic limitations, including: low photostability, small Stokes shifts, pronounced solvent-induced fluorescence quenching. To overcome these issues, Ren et al. introduced a strategy based on enhancing electronic asymmetry and increasing steric hindrance, leading to the development of solvent-resistant NIR-II dyes (NIR-II-RTs) with improved quantum yield and stability [107]. Notably, NIR-II-RT3/4 incorporates a carboxylic acid group that enables helical cyclization, resulting in an activatable NIR-II agent (Figure 9H). Performance evaluation (Figure 9I) shows that NIR-II-RT4 and NIR-II-RT1 exhibit fluorescence intensities approximately 3.6- to 10-fold higher than ICG, indicating significantly enhanced brightness and resistance to quenching. In vivo vascular imaging (Figure 9J) further demonstrates that NIR-II-RT1 enables clear discrimination between adjacent blood vessels, confirming its potential as a high-resolution NIR-II imaging agent. These findings highlight another important design rule: Increasing molecular rigidity and steric hindrance can effectively suppress non-radiative decay and fluorescence quenching.

Beyond imaging, D–A–D small-molecule fluorophores have also been engineered for PTT. For example, Yao et al. developed the NIR-II dye SQ1 by incorporating malonitrile into a D–A–D framework, achieving a photothermal efficiency of 25.6% [108]. In vivo experiments show that tumor temperatures increased from 33.2 to 59.1 °C upon laser irradiation, demonstrating effective photothermal performance. Similarly, Zeng et al. enhanced tumor targeting by conjugating the NIR-II dye H_2a-4T with cetuximab proteins and fetal bovine serum (FBS), resulting in improved accumulation in colorectal tumors and enhanced therapeutic outcomes [109]. These examples demonstrate that: functionalization with targeting ligands is critical for improving tumor specificity and therapeutic efficacy. Collectively, these studies highlight the growing structural diversity and functional engineering strategies of NIR-II fluorophores for photothermal applications. Nevertheless, more variety of NIR-II fluorescent dyes were developed and used for PTT applications with favorable photothermal performances [110,111], showcasing the potential uses of NIR-II dyes for imaging-guided PTT [112–114].

D–A–D small-molecule fluorophores and cyanine dyes provide a highly tunable platform for NIR-II imaging and therapy, with clear advantages in biocompatibility and clearance over inorganic systems. However, their performance strongly depends on precise molecular design. Strategies such as heteroatom engineering, donor–acceptor optimization, and structural rigidification are essential for achieving high brightness, stability, and deep-tissue imaging capability. Future development should focus on balancing optical performance, biological stability, and clinical safety to enable successful clinical translation.

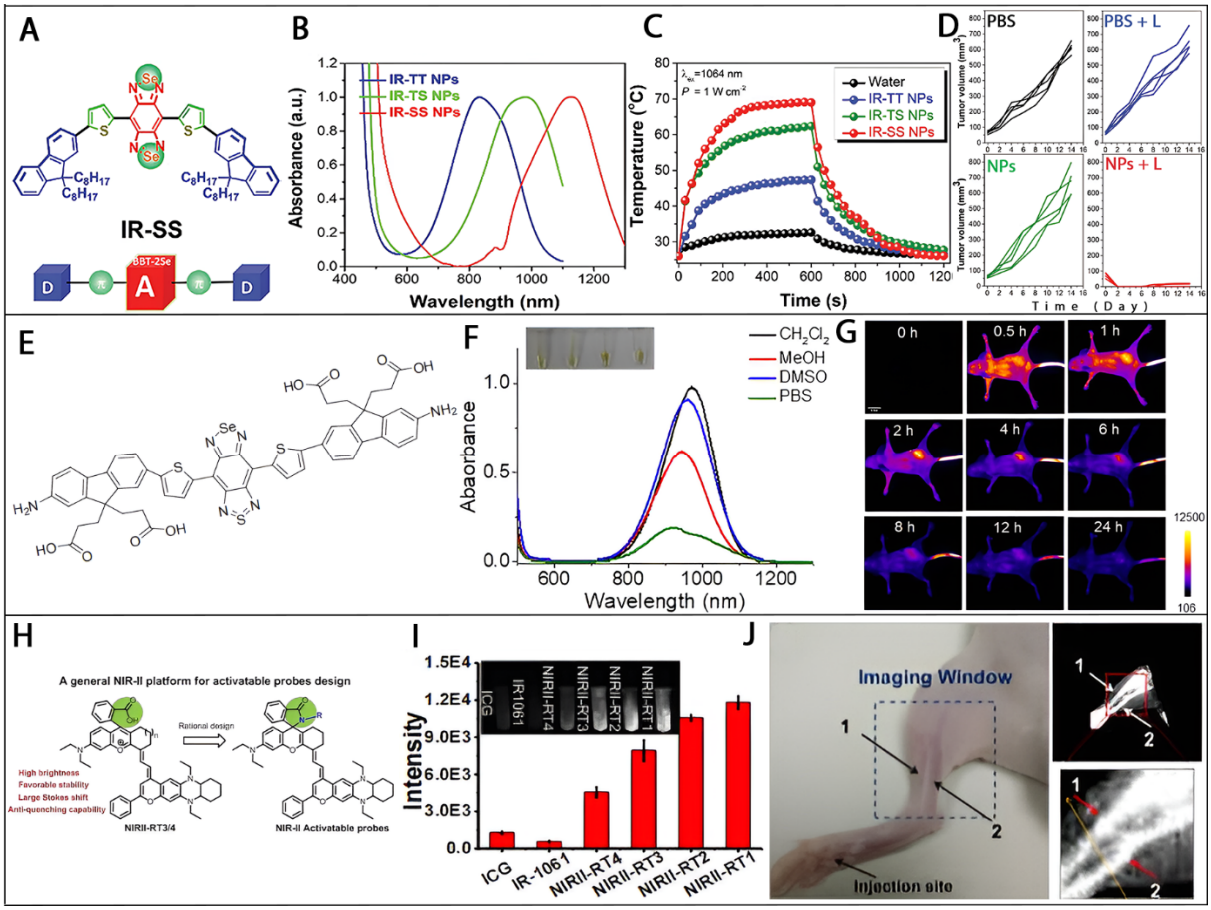

Figure 9. NIR-II application and synthesis process of conjugated polymers, benzobisthiadiazole, and cyanine dyes. (**A**) Molecular structures of IR-SS compounds. (**B**) UV–vis absorption spectra of IR-TT, TS, and SS nanoparticles. (**C**) Temperature change curves of IR-TT, IR-TS, and IR-SS nanoparticles at tumor sites under 1064 nm laser irradiation in different treatment groups (1.0 W cm^{-2}). (**D**) Tumor growth curves after different treatments over 14 days (Reprinted/adapted with permission from Ref. [96]. 2020, WILEY-VCH Verlag GmbH & Co. KGaA). (**E**) Molecular structure of FM1210. (**F**) UV–vis absorption spectra of FM1210. (**G**) Time-lapse in vivo imaging of mice after intravenous injection of FM1210-NPs (20 mg mL^{-1}, 100 µL); exposure time 150 ms, scale bar 5 mm (Reprinted/adapted with permission from Ref. [104]. 2020, American Chemical Society). (**H**) Molecular structure and synthesis process of NIRII-RT-pH nanoparticles. (**I**) NIR-II (1000–1700 nm) fluorescence brightness comparison of ICG, IR1061, and NIR-II-RT1–4 (5 µM) measured using an InGaAs camera in PBS (pH 7.4, 20% DMSO, 1% Tween-80); inset shows solution images. (**J**) In vivo NIR-II fluorescence imaging of vasculature in the mouse left hindlimb using NIR-II-RT1 (Reprinted/adapted with permission from Ref. [107]. 2020, Wiley-VCH GmbH).

5.3. Boron Dipyrromethene (BODIPY)-Based Fluorophores for NIR-II Applications

Boron dipyrromethene (BODIPY)-based fluorophores represent an important class of organic imaging agents due to their high fluorescence quantum yield, excellent photostability, and well-defined chemical structures. These intrinsic properties make them highly attractive for applications in drug delivery and molecular imaging. However, conventional BODIPY dyes typically exhibit absorption in the 500–600 nm range and relatively small Stokes shifts, which limit their direct applicability in NIR-II imaging. To overcome these limitations, molecular engineering strategies have been widely employed. Due to the strong electron-accepting nature of the BODIPY core, the incorporation of electron-donating substituents can effectively extend π-conjugation and promote intramolecular charge transfer, thereby red-shifting both absorption and emission wavelengths into the NIR windows [115,116]. As a result, various modified BODIPY derivatives, particularly aza-BODIPY systems, have been developed for NIR-II applications. Despite these advances, a major bottleneck for BODIPY-based fluorophores is their poor water solubility, which restricts their in vivo applicability and often necessitates additional encapsulation or surface modification. Addressing this issue, Godard et al. developed a hydrophilic aza-BODIPY derivative, SWIR-WAZABY-01, by introducing ammonium groups directly onto the boron center (Figure 10A) [117]. This structural modification significantly enhances aqueous solubility, eliminating the need for PEGylation or other encapsulation strategies. In vivo evaluation using U87MG tumor-bearing mice

demonstrated that SWIR-WAZABY-01 accumulates efficiently in tumor tissues following intravenous injection (Figure 10B). NIR-II imaging (Figure 10C) revealed clear tumor localization, with fluorescence signals gradually increasing and reaching peak tumor uptake at approximately 72 h post-injection. Notably, a maximum tumor-to-skin ratio of around 4 was achieved at 48 h, indicating strong imaging contrast. These results highlight a key design insight: Direct molecular functionalization (e.g., boron-site modification) is an effective strategy to improve water solubility without compromising optical performance. Furthermore, SWIR-WAZABY-01 exhibits prolonged tumor retention and favorable tumor-to-background ratios, suggesting its potential for long-term imaging applications. However, the relatively long retention time (up to several days) also raises considerations regarding clearance pathways and potential long-term accumulation, which are critical for clinical translation. In addition to SWIR-WAZABY-01, Bai et al. developed a series of aza-BODIPY dyes (NJ960, NJ1030, and NJ1060) that further extend emission into the NIR-II windows [116]. These dyes exhibit improved photophysical properties, including larger Stokes shifts, enhanced photostability, and strong fluorescence in aqueous environments. Among them, NJ1060 demonstrates particularly promising performance, enabling deep tissue penetration and high-resolution imaging in vivo. From a comparative perspective, BODIPY-based fluorophores occupy an intermediate position between traditional small-molecule dyes and conjugated polymer systems. While they offer higher structural precision and photostability than many cyanine dyes, they still face challenges in achieving sufficiently long emission wavelengths and optimal pharmacokinetics without additional modification.

Altogether, BODIPY-based NIR-II fluorophores provide a structurally well-defined and photostable platform for imaging applications. However, their performance is highly dependent on rational molecular modification, particularly in improving solubility and extending emission wavelengths. Strategies such as aza-modification, donor incorporation, and boron functionalization are essential for unlocking their full potential. Future work should focus on optimizing the balance between optical performance, solubility, and biological clearance to enable clinical translation.

5.4. Utilization of Other Small-Molecule Fluorophores for NIR-II Applications

To date, organic small-molecule dyes remain among the most widely used fluorescent agents for bioimaging due to their high fluorescence quantum yield, facile synthesis, and ease of functionalization. These dyes offer tunable optical properties and well-defined molecular structures, making them highly adaptable for biomedical applications [118–121]. However, most conventional dyes including rhodamines, anthocyanins, coumarins, fluoresceins, naphthalimides, porphyrins, and phthalocyanines primarily operate in the UV–visible or NIR-I windows, which limits their performance in deep-tissue imaging due to increased scattering and autofluorescence [122–124]. As a result, recent research has focused on structural remodeling and conjugation engineering to shift their optical properties into the NIR-II windows. A representative example is FD-1080, developed by Li et al. (2018) through structural modification of a conventional anthocyanin dye [125]. This small-molecule fluorophore exhibits excitation in the NIR-II windows under 1064 nm laser irradiation, with an emission peak at 1080 nm and a quantum yield of 5.94% (Figure 10D,E). Notably, imaging under 1064 nm laser irradiation produces significantly sharper and higher-resolution cerebrovascular images compared to lower-wavelength excitation (<980 nm), which results in blurred vascular structures (Figure 10F). Quantitative analysis based on the FWHM of vessel intensity profiles confirms that imaging at 1064 nm enables improved spatial resolution, demonstrating a key advantage of NIR-II excitation for reducing photon scattering and enhancing imaging clarity. These findings emphasize a central design principle: Extending excitation and emission wavelengths beyond 1000 nm significantly improves imaging depth and spatial resolution. FD-1080 further demonstrates excellent water solubility, high stability, and effective deep-tissue penetration, highlighting the potential of rationally engineered small-molecule dyes for NIR-II imaging applications. Another important example is indocyanine green (ICG), the only U.S. FDA-approved near-infrared fluorescent dye currently used in clinical practice. ICG is widely applied in cardiovascular imaging, liver function assessment, ophthalmic angiography, and cerebral imaging due to its low toxicity, rapid clearance, and strong absorption in the NIR-I windows.

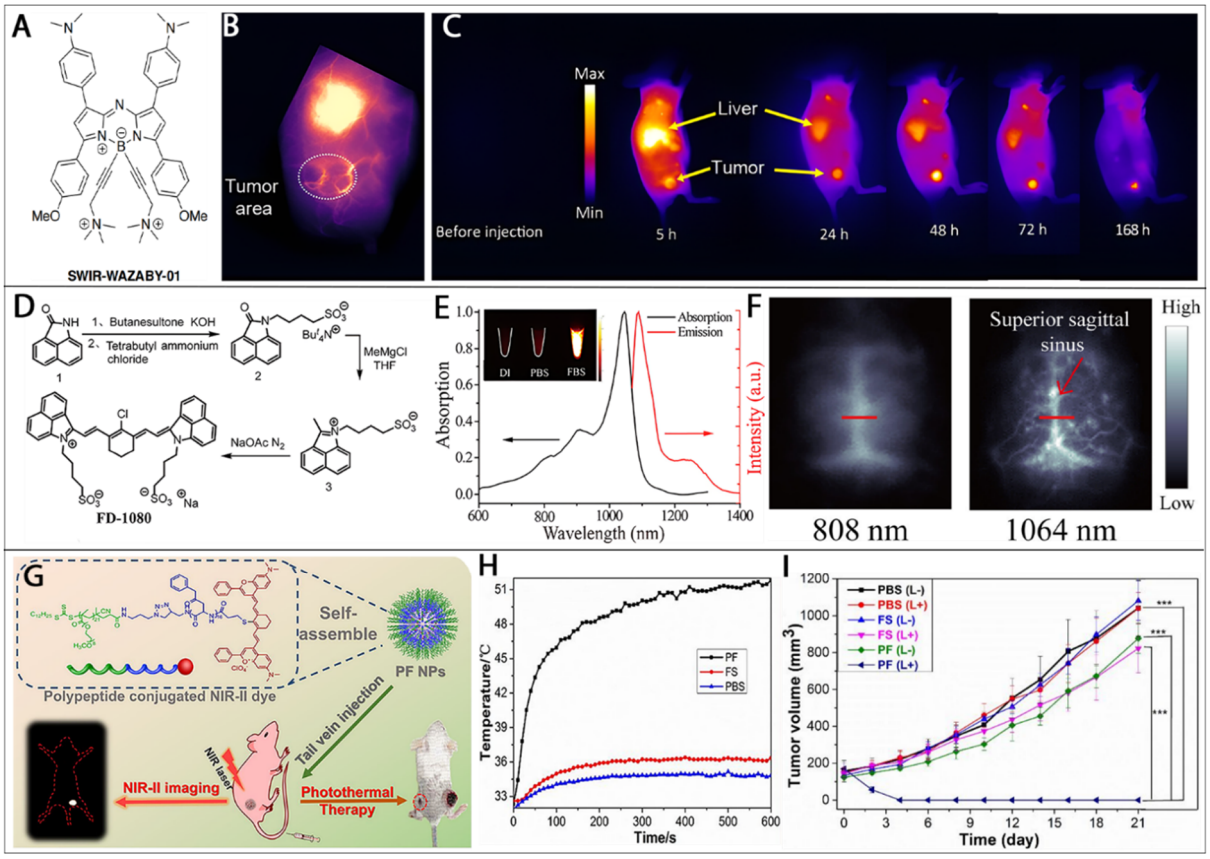

Figure 10. BODIPY-based and small-molecule NIR-II fluorophores for bioimaging and photothermal therapy. (**A**) Molecular structure of SWIR-WAZABY-01 and it's in vivo distribution in a U87MG tumor-bearing mouse at 1 min post-injection. (**B**,**C**) Time-lapse NIR-II imaging of SWIR-WAZABY-01 from 1 min to 7 days post-injection, acquired in the 1250–1700 nm range with 500 ms exposure intervals; biodistribution was analyzed between 24 and 168 h after injection (Reprinted/adapted with permission from Ref. [117]. 2020, American Chemical Society). (**D**) Synthetic route and molecular structure of FD-1080. (**E**) UV–vis absorption and fluorescence emission spectra of FD-1080, showing an absorption peak at ~1046 nm and emission peak at ~1080 nm; inset shows NIR-II fluorescence in deionized water, FBS, and PBS under 1064 nm laser irradiation (50 μM). (**F**) Comparison of brain vasculature fluorescence imaging using FD-1080 under 800 nm and 1064 nm laser irradiation (Reprinted/adapted with permission from Ref. [125]. 2018, Wiley-VCH Verlag GmbH & Co. KGaA). (**G**) Schematic illustration of the macromolecular nanoagent PF. (**H**) Temperature change curves of PBS, FS, and PF at tumor sites under 808 nm laser irradiation in different treatment groups (0.65 W cm^{-2}); treatment was administered once for in vivo photothermal therapy (n = 5). (**I**) Tumor growth curves after different treatment groups (Reprinted/adapted with permission from Ref. [126]. 2019, American Chemical Society).

Interestingly, Starosolski et al. demonstrated that ICG also exhibits fluorescence emission in the NIR-II windows under specific conditions [127]. This discovery significantly expands the clinical utility of ICG, enabling its application in NIR-II imaging without requiring the development of entirely new agents. Furthermore, the NIR-II optical emission behavior of ICG is highly dependent on its molecular environment (e.g., PBS, plasma, ethanol), indicating that microenvironmental interactions play a critical role in determining optical performance. This highlights another key insight: Repurposing clinically approved dyes through optical windows extension is a promising strategy for rapid clinical translation. Beyond imaging, small-molecule dyes have also been engineered for cancer theranostic applications, combining FLI and PTT. For example, Li et al. developed a macromolecular nanoagent (PF) by integrating a small-molecule NIR-II fluorophore (Flav7) with an amphiphilic polypeptide [126]. This hybrid system (Figure 10G) exhibits a high photothermal efficiency of 42.3%, along with excellent biocompatibility and photothermal stability. Under NIR laser irradiation, the PF-treated group shows a rapid temperature increase to 51.8 °C, whereas control groups (PBS and FS) exhibit minimal heating (Figure 10H). Correspondingly, tumor growth is significantly suppressed only in the PF + irradiation group ($p < 0.001$), while negligible effects are observed in control groups (Figure 10I). Importantly, no significant body weight changes are detected, indicating minimal systemic toxicity. These results demonstrate that: Hybridizing small-molecule dyes with macromolecular carriers enhances stability, tumor accumulation, and therapeutic performance. In addition,

other small-molecule dyes such as IR1048-MZ have also been explored for NIR-II imaging and therapy, further expanding the scope of this material class [128].

Taken together, small-molecule dye-based NIR-II fluorophores offer a highly promising pathway toward clinical translation due to their synthetic simplicity, tunable structures, and established safety profiles. While their intrinsic optical performance may be lower than that of some nanomaterials, strategies such as molecular engineering, environmental modulation, and hybrid system design can significantly enhance their functionality. Importantly, the ability to repurpose clinically approved dyes like ICG provides a practical and efficient route for accelerating the adoption of NIR-II imaging technologies in clinical translation.

6. Challenges for Clinical Translation

The clinical translation of metal-based NIR-II functional nanostructures remains challenging despite their promising biomedical applications. Although these materials have demonstrated strong performance in preclinical imaging and therapeutic applications, several key barriers limit their progression toward clinical use. These challenges include concerns related to biocompatibility and long-term toxicity, complex biodistribution and clearance behavior, and difficulties in achieving scalable and cost-effective production. Addressing these limitations is essential to improve the safety, reliability, and practical applicability of metal-based nanoplatforms. The major challenges and potential strategies for facilitating the clinical translation of NIR-II nanostructures are summarized in Figure 11.

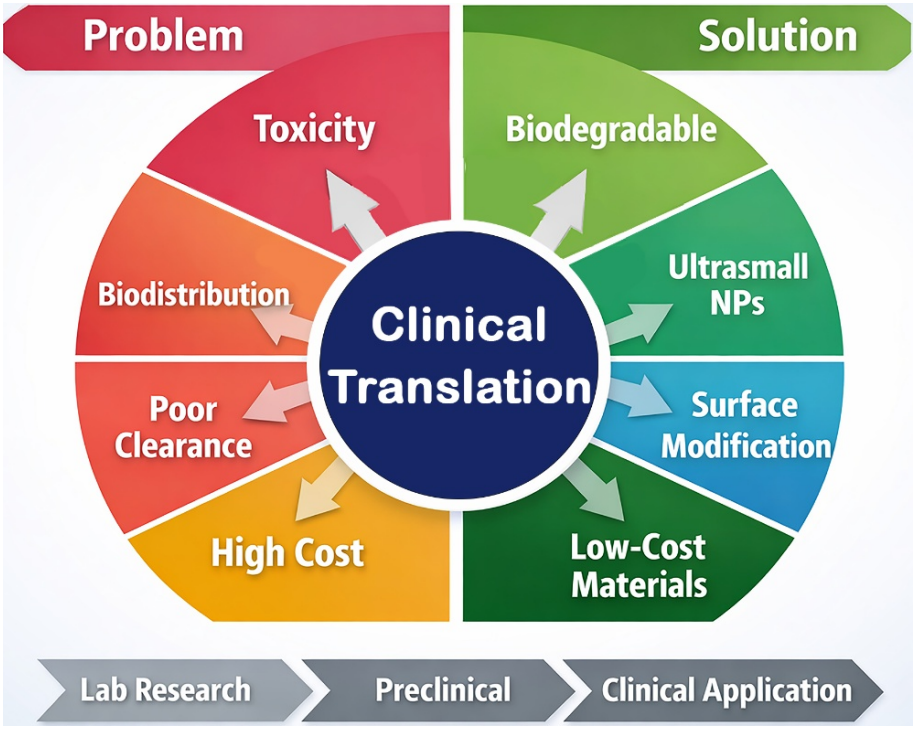

Figure 11. Schematic illustration of key challenges and potential solutions for the clinical translation of NIR-II functional nanostructures.

6.1. Long-Term Toxicity and Biocompatibility

The clinical translation of a wide range of nanostructures remains restricted by concerns regarding long-term toxicity, particularly due to their complex interactions with biological systems. Depending on their physicochemical properties, including size, shape, and surface chemistry, nanoparticles can overcome biological barriers and accumulate within cells and organelles, potentially inducing oxidative stress, inflammation, and cellular dysfunction [129]. Additionally, different immune cell populations may exhibit opposing activities, leading to either pro-inflammatory or anti-inflammatory responses, which makes immune interactions with biomaterials inherently unpredictable [130]. For instance, the biocompatibility of metal-based systems is strongly influenced by surface characteristics and microenvironmental conditions, which can modulate immune responses and ultimately affect their safety profiles [131]. In vivo studies have shown that many metal-based nanoparticles tend to accumulate in major organs such as the liver, spleen, lungs, and kidneys, with particle size, dosage, and surface modification playing critical roles in determining toxicity [132]. For example, conventional gold

nanoparticles often exhibit limited metabolic clearance and prolonged retention, whereas smaller gold nanoclusters with appropriate surface functionalization demonstrate reduced toxicity due to enhanced renal clearance pathways [133]. Similar challenges related to cytotoxicity and limited biodegradability are also observed in widely studied systems such as upconversion nanoparticles, highlighting the broader issue of insufficient degradability across different nanomaterial platforms [134]. In comparison, certain polymer-based or biodegradable nanomaterials generally exhibit improved biocompatibility and clearance behavior; however, they may compromise structural stability or functional performance under physiological conditions. This trade-off underscores the difficulty in simultaneously achieving high therapeutic efficacy and long-term biosafety.

Furthermore, prolonged in vivo retention of nanoparticles may result in chronic toxicity, particularly when clearance pathways are inefficient or incomplete [135]. Although NIR-II-based nanoplatforms have demonstrated promising therapeutic and imaging capabilities, they still face similar limitations, including the need to enhance biodegradability and minimize long-term toxicity for safe clinical applications [136]. While some nanostructures, such as bismuth-based nanoplates (e.g., Bi_2Se_3), exhibit favorable biocompatibility and gradual clearance, these findings are not universally applicable across all nanomaterial systems [137]. Therefore, comprehensive long-term in vivo evaluations, along with the rational design of biodegradable or metabolizable nanostructures, remain essential for advancing the clinical translation of metal-based NIR-II platforms.

6.2. Biodistribution and Clearance Mechanisms

The safety and clinical applicability of NIR-II nanostructures are strongly influenced by their biodistribution and clearance behavior. The RES rapidly recognizes and sequesters nanoparticles, leading to significant accumulation in the liver and spleen [132,137]. Such accumulation not only reduces therapeutic efficiency but also increases the risk of long-term toxicity. Importantly, nanoparticle physicochemical properties, including size, shape, and surface chemistry, play a decisive role in determining their in vivo fate. For example, nanoparticles with hydrodynamic diameters below ~5.5 nm can undergo efficient renal clearance, whereas larger particles are more likely to be retained within the body [138]. This size-dependent behavior highlights a fundamental design constraint in balancing effective tumor targeting with safe elimination. In line with this, studies on gold nanostructures demonstrate that surface chemistry critically influences clearance: glutathione-coated nanoclusters show efficient renal excretion, while protein-coated systems tend to accumulate in the liver and spleen [133]. Surface modification strategies further affect biodistribution patterns. PEGylated nanoparticles generally exhibit improved colloidal stability and prolonged circulation, which may enhance tumor accumulation, but they can also undergo hepatobiliary clearance depending on their size and composition. In contrast, aggregated or poorly stabilized systems are more prone to rapid sequestration and long-term retention, increasing potential toxicity risks [139]. In addition, achieving an optimal balance between tumor retention and systemic clearance remains a major challenge. While many nanoplatforms are designed to exploit EPR effect for passive tumor targeting, the variability of the EPR effect across different tumor types and patients limits its reliability in clinical settings [140]. Moreover, many NIR-II nanostructures still exhibit inefficient clearance and prolonged organ retention, which continues to hinder their clinical translation [135].

Overall, these limitations highlight the need for rational and standardized design strategies to precisely control biodistribution and promote efficient excretion. Comparative evaluation across different nanomaterial systems suggests that smaller, surface-engineered, and biodegradable platforms may offer improved clearance profiles; however, these advantages must be carefully balanced against potential losses in stability and therapeutic performance.

6.3. Cost, Scalability, and Manufacturing Challenges

Beyond biological barriers, the clinical translation of NIR-II nanostructures is significantly constrained by manufacturing and economic challenges. The large-scale production of noble metal-based materials, such as gold and platinum, is often limited by complex, multi-step synthesis processes and their inherently high cost [141]. In addition, maintaining uniformity and reproducibility during scale-up remains difficult, as nanocrystal nucleation and growth are highly sensitive to reaction conditions, including temperature, precursor concentration, and reaction time [142]. The complexity of nanoparticle formulations further increases production costs and reduces their practical feasibility compared to conventional therapeutic systems [143]. In particular, multifunctional and hybrid nanoplatforms, while offering enhanced therapeutic performance, typically require more sophisticated fabrication procedures, which complicates large-scale manufacturing and quality control. In contrast, relatively simpler nanostructures or polymer-based systems may offer improved scalability and cost-effectiveness, although they can be limited in terms of stability or functional performance. Moreover, additional challenges such as batch-to-batch variability, limited stability during storage, and short shelf-life under standard conditions further hinder their

practical application. For example, many nanoparticle-based systems require strict cold-chain storage, which increases logistical complexity and cost during transportation and clinical use [59].

Collectively, these issues restrict the large-scale production and widespread adoption of metal-based NIR-II nanomaterials. Therefore, the development of cost-effective, reproducible, and scalable synthesis strategies, along with standardized manufacturing protocols, is essential to facilitate their successful clinical translation.

6.4. Future Perspectives and Potential Solutions

Addressing the challenges associated with clinical translation requires a multidisciplinary approach that integrates rational material design, comprehensive biological evaluation, and well-defined regulatory frameworks. Similar translational barriers have also been observed in other advanced therapeutic platforms, such as exosome-based systems, where issues related to heterogeneity, safety, and scalability necessitate standardized engineering and evaluation strategies [144]. These parallels highlight that many of the current limitations are not unique to NIR-II nanomaterials but reflect broader challenges in nanomedicine development. One key direction involves the development of biocompatible and biodegradable nanomaterials to minimize long-term toxicity and improve clearance profiles. Surface engineering strategies, including functional coatings and ligand modifications, have demonstrated potential in enhancing targeting efficiency while reducing nonspecific protein adsorption and immune recognition [145]. In addition, advanced nanoparticle designs, such as stimuli-responsive systems and multifunctional platforms, may improve therapeutic efficacy; however, their increased structural complexity can introduce additional challenges in reproducibility and large-scale manufacturing [146]. The establishment of standardized evaluation protocols for toxicity, biodistribution, and pharmacokinetics is also essential to ensure reproducibility and facilitate regulatory approval. At present, the lack of consistent preclinical models, along with the limited correlation between in vitro and in vivo results, remains a significant obstacle in accurately predicting clinical outcomes [147,148]. In addition, overcoming regulatory and translational barriers will require closer collaboration among academic researchers, industry stakeholders, and regulatory agencies to establish clear guidelines and accelerate clinical validation.

Overall, future efforts should focus on the development of scalable, cost-effective, and clinically translatable nanoplatforms, thereby narrowing the gap between laboratory research and real-world biomedical applications.

7. Conclusions

In conclusion, NIR-II-responsive nanomaterials have emerged as a highly promising platform for advanced cancer theranostics, offering significant advantages in deep-tissue imaging, reduced photon scattering, and high signal-to-noise ratios compared with conventional imaging modalities. This review systematically highlights the rapid progress across multiple classes of NIR-II nanostructures, including metal-based nanomaterials, alloy systems, 2D materials, hybrid/composite platforms, semiconductor and carbon-based nanomaterials, as well as organic fluorophores. Collectively, these systems demonstrate that rational control over composition, morphology, and surface engineering is crucial for optimizing optical performance and therapeutic efficiency in the NIR-II windows. Among them, metal-based and alloy nanostructures exhibit outstanding photothermal efficiency and tunable LSPR, while 2D materials provide large surface areas and efficient light-to-heat conversion. Hybrid and composite systems further integrate multiple functionalities, enabling synergistic imaging and therapy. In parallel, carbon-based and semiconductor nanomaterials offer improved biocompatibility and tunable optical properties, whereas organic fluorophores stand out for their well-defined structures, biodegradability, and clinical potential. These diverse material platforms collectively enable multimodal imaging and combined therapeutic strategies, including FLI, PTT, PDT, and chemo-photothermal synergistic treatments. Despite these advances, several critical challenges remain for clinical translation. Issues such as long-term toxicity, non-specific biodistribution, limited clearance, high production cost, and scalability continue to hinder practical application. In particular, nanoparticle accumulation in the reticuloendothelial system and insufficient biodegradability raises safety concerns, emphasizing the need for size-controlled, surface-engineered, and metabolizable nanoplatforms. Looking forward, future research should focus on the development of biocompatible and biodegradable materials, precise control of pharmacokinetics, and scalable synthesis strategies, alongside the establishment of standardized evaluation protocols for toxicity and efficacy. Moreover, interdisciplinary collaboration between materials science, biology, and clinical research will be essential to accelerate regulatory approval and real-world implementation. Overall, NIR-II nanostructures hold immense potential to revolutionize cancer diagnosis and treatment. With continued innovation and careful consideration of translational challenges, these nanoplatforms are expected to bridge the gap between laboratory research and clinical application, paving the way for safer, more effective, and personalized cancer theranostics.

Author Contributions

E.H. and J.L.: Data curation, Investigation, Methodology, Resources, Writing—original draft; X.Z. and X.G.: formal analysis, investigation, methodology, formal analysis, resources, software, visualization; Z.W. and X.M.: Conceptualization, Funding acquisition, Data curation, Funding acquisition, Supervision, Writing—review & editing. All authors have read and agreed to the published version of the manuscript.

Funding

This work was supported by the Chongqing Municipal Natural Science Foundation: (CSTB2022NSCQ-MSX0113); the Science and Technology Research Program of Chongqing Municipal Education Commission (KJZD-K202500411).

Institutional Review Board Statement

Not applicable.

Informed Consent Statement

Not applicable.

Data Availability Statement

All data supporting the conclusions of this review article are available in the published literature cited in the reference list. No new original data were generated or analyzed in this study.

Conflicts of Interest

The authors declare no conflict of interest.

Use of AI and AI-Assisted Technologies

No AI tools were used directly in the preparation of this manuscript. AI-based tools were occasionally consulted for general ideas and improvement suggestions; however, all content was written, reviewed, and finalized by the author(s), who take full responsibility for the manuscript.

References

1. Torre, L.A.; Trabert, B.; DeSantis, C.E.; et al. Ovarian cancer statistics, 2018. *CA Cancer J. Clin.* **2018**, *68*, 284–296.
2. Yang, Q.; Ma, Z.; Wang, H.; et al. Rational design of molecular fluorophores for biological imaging in the NIR-II window. *Adv. Mater.* **2017**, *29*, 1605497.
3. Chen Y, Sun B, Jiang X; et al. Double-acceptor conjugated polymers for NIR-II fluorescence imaging and NIR-II photothermal therapy applications. *J. Mater. Chem. B* **2021**, *9*, 1002–1008.
4. Suo Y, Wu F, Xu P; et al. NIR-II fluorescence endoscopy for targeted imaging of colorectal cancer. *Adv. Healthc. Mater.* **2019**, *8*, 1900974.
5. Liu, Y.; Bhattarai, P.; Dai, Z.; et al. Photothermal therapy and photoacoustic imaging via nanotheranostics in fighting cancer. *Chem. Soc. Rev.* **2019**, *48*, 2053–2108.
6. Yuan, S.; Zhao, Y.; Liu, S.; et al. Optical imaging probes for mitochondrial metabolism: Mechanism, design and frontier applications. *Coord. Chem. Rev.* **2026**, *553*, 217570.
7. Hilderbrand, S.A.; Weissleder, R. Near-infrared fluorescence: Application to in vivo molecular imaging. *Curr. Opin. Chem. Biol.* **2010**, *14*, 71–79.
8. Chen, G.; Qiu, H.; Prasad, P.N.; et al. Upconversion nanoparticles: Design, nanochemistry, and applications in theranostics. *Chem. Rev.* **2014**, *114*, 5161–5214.
9. Sevick-Muraca, E.M.; Houston, J.P.; Gurfinkel, M. Fluorescence-enhanced, near infrared diagnostic imaging with contrast agents. *Curr. Opin. Chem. Biol.* **2002**, *6*, 642–650.
10. Cao, J.; Zhu, B.; Zheng, K.; et al. Recent progress in NIR-II contrast agent for biological imaging. *Front. Bioeng. Biotechnol.* **2020**, *7*, 487.
11. Hu, Z.; Fang, C.; Li, B.; et al. First-in-human liver-tumour surgery guided by multispectral fluorescence imaging in the visible and near-infrared-I/II windows. *Nat. Biomed. Eng.* **2020**, *4*, 259–271.
12. Zhen, X.; Pu, K.; Jiang, X. Photoacoustic imaging and photothermal therapy of semiconducting polymer nanoparticles: Signal amplification and second near-infrared construction. *Small* **2021**, *17*, 2004723.

13. Wen, G.; Li, X.; Zhang, Y.; et al. Effective phototheranostics of brain tumor assisted by near-infrared-II light-responsive semiconducting polymer nanoparticles. *ACS Appl. Mater. Interfaces* **2020**, *12*, 33492–33499.
14. Zhu, P.; Gao, S.; Lin, H.; et al. Inorganic nanoshell-stabilized liquid metal for targeted photonanomedicine in NIR-II biowindow. *Nano Lett.* **2019**, *19*, 2128–2137.
15. Sun, T.; Han, J.; Liu, S.; et al. Tailor-made semiconducting polymers for second near-infrared photothermal therapy of orthotopic liver cancer. *ACS Nano* **2019**, *13*, 7345–7354.
16. Hu, K.; Xie, L.; Zhang, Y.; et al. Marriage of black phosphorus and Cu^{2+} as effective photothermal agents for PET-guided combination cancer therapy. *Nat. Commun.* **2020**, *11*, 2778.
17. Zha, Z.; Yue, X.; Ren, Q.; et al. Uniform polypyrrole nanoparticles with high photothermal conversion efficiency for photothermal ablation of cancer cells. *Adv. Mater.* **2012**, *25*, 777–782.
18. Hu, X.; Lu, Y.; Dong, C.; et al. A RuII Polypyridyl Alkyne Complex Based Metal–Organic Frameworks for Combined Photodynamic/Photothermal/Chemotherapy. *Chem. Eur. J.* **2020**, *26*, 1668–1675.
19. Li, Z.; Hu, Y.; Jiang, T.; et al. Human-serum-albumin-coated prussian blue nanoparticles as pH-/thermotriggered drug-delivery vehicles for cancer thermochemotherapy. *Part. Part. Syst. Charact.* **2016**, *33*, 53–62.
20. Li, X.; Lovell, J.F.; Yoon, J.; et al. Clinical development and potential of photothermal and photodynamic therapies for cancer. *Nat. Rev. Clin. Oncol.* **2020**, *17*, 657–674.
21. Tang, B.; Li, W.L.; Chang, Y.; et al. A supramolecular radical dimer: High-efficiency NIR-II photothermal conversion and therapy. *Angew. Chem. Int. Ed.* **2019**, *58*, 15526–15531.
22. Huang, J.; Huang, Y.; Xue, Z.; et al. Tumor microenvironment responsive hollow mesoporous Co_9S_8@ MnO_2-ICG/DOX intelligent nanoplatform for synergistically enhanced tumor multimodal therapy. *Biomaterials* **2020**, *262*, 120346.
23. Zhang, Y.; Zhang, S.; Zhang, Z.; et al. Recent progress on NIR-II photothermal therapy. *Front. Chem.* **2021**, *9*, 728066.
24. Jeevanandam P, Mulukutla R, Phillips M; et al. Near infrared reflectance properties of metal oxide nanoparticles. *J. Phys. Chem. C* **2007**, *111*, 1912–1918.
25. Yang, N.; Gong, F.; Zhou, Y.; et al. A general in-situ reduction method to prepare core-shell liquid-metal/metal nanoparticles for photothermally enhanced catalytic cancer therapy. *Biomaterials* **2021**, *277*, 121125.
26. Paramasivam, G.; Kayambu, N.; Rabel, A.M.; et al. Anisotropic noble metal nanoparticles: Synthesis, surface functionalization and applications in biosensing, bioimaging, drug delivery and theranostics. *Acta Biomater.* **2017**, *49*, 45–65.
27. Kuchur, O.; Tsymbal, S.; Shestovskaya, M.; et al. Metal-derived nanoparticles in tumor theranostics: Potential and limitations. *J. Inorg. Biochem.* **2020**, *209*, 111117.
28. Liu, Y.; Zhang, X.; Luo, L.; et al. Self-assembly of stimuli-responsive Au–Pd bimetallic nanoflowers based on betulinic acid liposomes for synergistic chemo-photothermal cancer therapy. *ACS Biomater. Sci. Eng.* **2018**, *4*, 2911–2921.
29. Li, L.; Chen, C.; Liu, H.; et al. Multifunctional carbon–silica nanocapsules with gold core for synergistic photothermal and chemo-cancer therapy under the guidance of bimodal imaging. *Adv. Funct. Mater.* **2016**, *26*, 4252–4261.
30. Luo, L.; Sun, W.; Feng, Y.; et al. Conjugation of a scintillator complex and gold nanorods for dual-modal image-guided photothermal and X-ray-induced photodynamic therapy of tumors. *ACS Appl. Mater. Interfaces* **2020**, *12*, 12591–12599.
31. Sangnier, A.P.; Aufaure, R.; Cheong, S.; et al. Raspberry-like small multicore gold nanostructures for efficient photothermal conversion in the first and second near-infrared windows. *Chem. Commun.* **2019**, *55*, 4055–4058.
32. Wang, Z.; Ju, Y.; Tong, S.; et al. Au 3 Cu tetrapod nanocrystals: Highly efficient and metabolizable multimodality imaging-guided NIR-II photothermal agents. *Nanoscale Horiz.* **2018**, *3*, 624–631.
33. Gao, F.; He, G.; Yin, H.; et al. Titania-coated 2D gold nanoplates as nanoagents for synergistic photothermal/sonodynamic therapy in the second near-infrared window. *Nanoscale* **2019**, *11*, 2374–2384.
34. Song, C.; Li, F.; Guo, X.; et al. Gold nanostars for cancer cell-targeted SERS-imaging and NIR light-triggered plasmonic photothermal therapy (PPTT) in the first and second biological windows. *J. Mater. Chem. B* **2019**, *7*, 2001–2008.
35. Yang, H.; He, H.; Tong, Z.; et al. The impact of size and surface ligand of gold nanorods on liver cancer accumulation and photothermal therapy in the second near-infrared window. *J. Colloid Interface Sci.* **2020**, *565*, 186–196.
36. Wang, J.; Sun, J.; Wang, Y.; et al. Gold nanoframeworks with mesopores for Raman–photoacoustic imaging and photo-chemo tumor therapy in the second near-infrared biowindow. *Adv. Funct. Mater.* **2020**, *30*, 1908825.
37. Liu, H.; Chen, D.; Li, L.; et al. Multifunctional gold nanoshells on silica nanorattles: A platform for the combination of photothermal therapy and chemotherapy with low systemic toxicity. *Angew. Chem.* **2011**, *123*, 921–925.
38. Wu, Z.; Yao, Q.; Chai, O.J.H.; et al. Unraveling the impact of gold (I)–thiolate motifs on the aggregation-induced emission of gold nanoclusters. *Angew. Chem.* **2020**, *132*, 10020–10025.
39. Yang, Y.; Yu, Y.; Chen, H.; et al. Illuminating platinum transportation while maximizing therapeutic efficacy by gold nanoclusters via simultaneous near-infrared-I/II imaging and glutathione scavenging. *ACS Nano* **2020**, *14*, 13536–13547.
40. Ding, X.; Liow, C.H.; Zhang, M.; et al. Surface plasmon resonance enhanced light absorption and photothermal therapy in the second near-infrared window. *J. Am. Chem. Soc.* **2014**, *136*, 15684–15693.

41. Ferrando, R.; Jellinek, J.; Johnston, R.L. Nanoalloys: From theory to applications of alloy clusters and nanoparticles. *Chem. Rev.* **2008**, *108*, 845–910.
42. Andolina, C.M.; Dewar, A.C.; Smith, A.M.; et al. Photoluminescent gold–copper nanoparticle alloys with composition-tunable near-infrared emission. *J. Am. Chem. Soc.* **2013**, *135*, 5266–5269.
43. Marbella, L.E.; Andolina, C.M.; Smith, A.M.; et al. Gold-cobalt nanoparticle alloys exhibiting tunable compositions, near-infrared emission, and high T2 relaxivity. *Adv. Funct. Mater.* **2014**, *24*, 6532–6539.
44. Wang, G.; Guo, R.; Kalyuzhny, G.; et al. NIR luminescence intensities increase linearly with proportion of polar thiolate ligands in protecting monolayers of Au38 and Au140 quantum dots. *J. Phys. Chem. B* **2006**, *110*, 20282–20289.
45. Zheng, J.; Zhang, C.; Dickson, R.M. Highly fluorescent, water-soluble, size-tunable gold quantum dots. *Phys. Rev. Lett.* **2004**, *93*, 077402.
46. Zheng, J.; Zhou, C.; Yu, M.; et al. Different sized luminescent gold nanoparticles. *Nanoscale* **2012**, *4*, 4073–4083.
47. Christensen, A.; Ruban, A.; Stoltze, P.; et al. Phase diagrams for surface alloys. *Phys. Rev. B* **1997**, *56*, 5822.
48. Crespo, O.; Gimeno, M.C.; Laguna, A.; et al. Highly luminescent gold (I)–silver (I) and gold (I)–copper (I) chalcogenide clusters. *Chem. Eur. J.* **2007**, *13*, 235–246.
49. Xie, H.; Li, Z.; Sun, Z.; et al. Metabolizable ultrathin Bi_2Se_3 nanosheets in imaging-guided photothermal therapy. *Small* **2016**, *12*, 4136–4145.
50. Xing, C.; Jing, G.; Liang, X.; et al. Graphene oxide/black phosphorus nanoflake aerogels with robust thermo-stability and significantly enhanced photothermal properties in air. *Nanoscale* **2017**, *9*, 8096–8101.
51. Geng, B.; Shen, W.; Li, P.; et al. Carbon dot-passivated black phosphorus nanosheet hybrids for synergistic cancer therapy in the NIR-II window. *ACS Appl. Mater. Interfaces* **2019**, *11*, 44949–44960.
52. Lin, H.; Gao, S.; Dai, C.; et al. A two-dimensional biodegradable niobium carbide (MXene) for photothermal tumor eradication in NIR-I and NIR-II biowindows. *J. Am. Chem. Soc.* **2017**, *139*, 16235–16247.
53. Lin, S.; Lin, H.; Yang, M.; et al. A two-dimensional MXene potentiates a therapeutic microneedle patch for photonic implantable medicine in the second NIR biowindow. *Nanoscale* **2020**, *12*, 10265–10276.
54. Zhou, Z.; Li, B.; Shen, C.; et al. Metallic 1T phase enabling MoS_2 nanodots as an efficient agent for photoacoustic imaging guided photothermal therapy in the near-infrared-ii window. *Small* **2020**, *16*, 2004173.
55. Cheng, Y.; Yang, F.; Xiang, G.; et al. Ultrathin tellurium oxide/ammonium tungsten bronze nanoribbon for multimodality imaging and second near-infrared region photothermal therapy. *Nano Lett.* **2019**, *19*, 1179–1189.
56. Yang, C.; Chan, K.K.; Xu, G.; et al. Biodegradable polymer-coated multifunctional graphene quantum dots for light-triggered synergetic therapy of pancreatic cancer. *ACS Appl. Mater. Interfaces* **2018**, *11*, 2768–2781.
57. Cui, X.; Li, M.; Wei, F.; et al. Biomimetic light-activatable graphene-based nanoarchitecture for synergistic chemophotothermal therapy. *Chem. Eng. J.* **2021**, *420*, 127710.
58. Xu, Z.; Zhang, Y.; Zhou, W.; et al. NIR-II-activated biocompatible hollow nanocarbons for cancer photothermal therapy. *J. Nanobiotechnol.* **2021**, *19*, 137.
59. O'Shea, D.; Hodgkinson, T.; Dixon, J.; et al. Development of an 'Off-the-Shelf'Gene therapeutic nanoparticle formulation for incorporation into biomaterials for regenerative medicine applications. *Eur. Cell Mater.* **2024**, *47*, 152–169.
60. O'connell, M.J.; Bachilo, S.M.; Huffman, C.B.; et al. Band gap fluorescence from individual single-walled carbon nanotubes. *Science* **2002**, *297*, 593–596.
61. Robinson, J.T.; Welsher, K.; Tabakman, S.M.; et al. High performance in vivo near-IR (>1 μm) imaging and photothermal cancer therapy with carbon nanotubes. *Nano Res.* **2010**, *3*, 779–793.
62. Takeuchi, T.; Iizumi, Y.; Yudasaka, M.; et al. Characterization and biodistribution analysis of oxygen-doped single-walled carbon nanotubes used as in vivo fluorescence imaging probes. *Bioconjug. Chem.* **2019**, *30*, 1323–1330.
63. Yi, H.; Ghosh, D.; Ham, M.-H.; et al. M13 phage-functionalized single-walled carbon nanotubes as nanoprobes for second near-infrared window fluorescence imaging of targeted tumors. *Nano Lett.* **2012**, *12*, 1176–1183.
64. Murakami, T.; Nakatsuji, H.; Inada, M.; et al. Photodynamic and photothermal effects of semiconducting and metallic-enriched single-walled carbon nanotubes. *J. Am. Chem. Soc.* **2012**, *134*, 17862–17865.
65. Hong, G.; Diao, S.; Chang, J.; et al. Through-skull fluorescence imaging of the brain in a new near-infrared window. *Nat. Photonics* **2014**, *8*, 723–730.
66. Hong, G.; Lee, J.C.; Robinson, J.T.; et al. Multifunctional in vivo vascular imaging using near-infrared II fluorescence. *Nat. Med.* **2012**, *18*, 1841–1846.
67. Welsher, K.; Sherlock, S.P.; Dai, H. Deep-tissue anatomical imaging of mice using carbon nanotube fluorophores in the second near-infrared window. *Proc. Natl. Acad. Sci. USA* **2011**, *108*, 8943–8948.
68. Zheng, M.; Jagota, A.; Semke, E.D.; et al. DNA-assisted dispersion and separation of carbon nanotubes. *Nat. Mater.* **2003**, *2*, 338–342.
69. Ghosh, D.; Bagley, A.F.; Na, Y.J.; et al. Deep, noninvasive imaging and surgical guidance of submillimeter tumors using targeted M13-stabilized single-walled carbon nanotubes. *Proc. Natl. Acad. Sci. USA* **2014**, *111*, 13948–13953.

70. Chen, J.; Wang, M.; Xi, B.; et al. SPARC is a key regulator of proliferation, apoptosis and invasion in human ovarian cancer. *PLoS ONE* **2012**, *7*, e42413.
71. Iizumi, Y.; Yudasaka, M.; Kim, J.; et al. Oxygen-doped carbon nanotubes for near-infrared fluorescent labels and imaging probes. *Sci. Rep.* **2018**, *8*, 6272.
72. Liu, Z.; Davis, C.; Cai, W.; et al. Circulation and long-term fate of functionalized, biocompatible single-walled carbon nanotubes in mice probed by Raman spectroscopy. *Proc. Natl. Acad. Sci. USA* **2008**, *105*, 1410–1415.
73. Welsher, K.; Liu, Z.; Sherlock, S.P.; et al. A route to brightly fluorescent carbon nanotubes for near-infrared imaging in mice. *Nat. Nanotechnol.* **2009**, *4*, 773–780.
74. Geng, B.; Shen, W.; Fang, F.; et al. Enriched graphitic N dopants of carbon dots as F cores mediate photothermal conversion in the NIR-II window with high efficiency. *Carbon* **2020**, *162*, 220–233.
75. Wang, H.; Pan, X.; Wang, X.; et al. Degradable carbon–silica nanocomposite with immunoadjuvant property for dual-modality photothermal/photodynamic therapy. *ACS Nano* **2020**, *14*, 2847–2859.
76. Sun, W.; Zhang, X.; Jia, H.R.; et al. Water-dispersible candle soot–derived carbon nano-onion clusters for imaging-guided photothermal cancer therapy. *Small* **2019**, *15*, 1804575.
77. Lu, G.-H.; Shang, W.-T.; Deng, H.; et al. Targeting carbon nanotubes based on IGF-1R for photothermal therapy of orthotopic pancreatic cancer guided by optical imaging. *Biomaterials* **2019**, *195*, 13–22.
78. Li, Y.; Bai, G.; Zeng, S.; et al. Theranostic carbon dots with innovative NIR-II emission for in vivo renal-excreted optical imaging and photothermal therapy. *ACS Appl. Mater. Interfaces* **2019**, *11*, 4737–4744.
79. Permatasari, F.A.; Fukazawa, H.; Ogi, T.; et al. Design of pyrrolic-N-rich carbon dots with absorption in the first near-infrared window for photothermal therapy. *ACS Appl. Nano Mater.* **2018**, *1*, 2368–2375.
80. Gong, P.; Guo, L.; Pang, M.; et al. Nano-sized paramagnetic and fluorescent fluorinated carbon fiber with high NIR absorbance for cancer chemo-photothermal therapy. *J. Mater. Chem. B* **2018**, *6*, 3068–3077.
81. Geng, B.; Yang, D.; Pan, D.; et al. NIR-responsive carbon dots for efficient photothermal cancer therapy at low power densities. *Carbon* **2018**, *134*, 153–162.
82. Thakur, M.; Kumawat, M.K.; Srivastava, R. Multifunctional graphene quantum dots for combined photothermal and photodynamic therapy coupled with cancer cell tracking applications. *RSC Adv.* **2017**, *7*, 5251–5261.
83. Cao, Y.; Li, S.; Chen, C.; et al. Rattle-type Au@Cu_2−xS hollow mesoporous nanocrystals with enhanced photothermal efficiency for intracellular oncogenic microRNA detection and chemo-photothermal therapy. *Biomaterials* **2018**, *158*, 23–33.
84. Zhao, Y.; Song, Z. Phase transfer-based synthesis of highly stable, biocompatible and the second near-infrared-emitting silver sulfide quantum dots. *Mater. Lett.* **2014**, *126*, 78–80.
85. Yang, H.-Y.; Zhao, Y.-W.; Zhang, Z.-Y.; et al. One-pot synthesis of water-dispersible Ag_2S quantum dots with bright fluorescent emission in the second near-infrared window. *Nanotechnol.* **2013**, *24*, 055706.
86. Matea, C.T.; Mocan, T.; Tabaran, F.; et al. Quantum dots in imaging, drug delivery and sensor applications. *Int. J. Nanomed.* **2017**, *12*, 5421–5431.
87. Hong, G.; Robinson, J.T.; Zhang, Y.; et al. In vivo fluorescence imaging with Ag_2S quantum dots in the second near-infrared region. *Angew. Chem. Int. Ed.* **2012**, *51*, 9818–9821.
88. Zhang, Y.; Hong, G.; Zhang, Y.; et al. Ag_2S quantum dot: A bright and biocompatible fluorescent nanoprobe in the second near-infrared window. *ACS Nano* **2012**, *6*, 3695–3702.
89. Zhang, Y.; Zhang, Y.; Hong, G.; et al. Biodistribution, pharmacokinetics and toxicology of Ag_2S near-infrared quantum dots in mice. *Biomaterials* **2013**, *34*, 3639–3646.
90. Shen, S.; Zhang, Y.; Peng, L.; et al. Matchstick-Shaped Ag_2S–ZnS Heteronanostructures Preserving both UV/Blue and Near-Infrared Photoluminescence. *Angew. Chem. Int. Ed.* **2011**, *50*, 7115–7118.
91. Du, Y.; Xu, B.; Fu, T.; et al. Near-infrared photoluminescent Ag_2S quantum dots from a single source precursor. *J. Am. Chem. Soc.* **2010**, *132*, 1470–1471.
92. Gao, X.; Cui, Y.; Levenson, R.M.; et al. In vivo cancer targeting and imaging with semiconductor quantum dots. *Nat. Biotechnol.* **2004**, *22*, 969–976.
93. Mahesh, M. The essential physics of medical imaging. *Med. Phys.* **2013**, *40*, 077301.
94. Guo, W.; Qiu, Z.; Guo, C.; et al. Multifunctional theranostic agent of $Cu_2(OH)PO_4$ quantum dots for photoacoustic image-guided photothermal/photodynamic combination cancer therapy. *ACS Appl. Mater. Interfaces* **2017**, *9*, 9348–9358.
95. Liu, H.; Li, C.; Qian, Y.; et al. Magnetic-induced graphene quantum dots for imaging-guided photothermal therapy in the second near-infrared window. *Biomaterials* **2020**, *232*, 119700.
96. Li, S.; Deng, Q.; Zhang, Y.; et al. Rational design of conjugated small molecules for superior photothermal theranostics in the NIR-II biowindow. *Adv. Mater.* **2020**, *32*, 2001146.
97. Liu, Z.; Qiu, K.; Liao, X.; et al. Nucleus-targeting ultrasmall ruthenium (iv) oxide nanoparticles for photoacoustic imaging and low-temperature photothermal therapy in the NIR-II window. *Chem. Commun.* **2020**, *56*, 3019–3022.

98. Guo, B.; Sheng, Z.; Hu, D.; et al. Through scalp and skull NIR-II photothermal therapy of deep orthotopic brain tumors with precise photoacoustic imaging guidance. *Adv. Mater.* **2018**, *30*, 1802591.
99. Cao, Z.; Feng, L.; Zhang, G.; et al. Semiconducting polymer-based nanoparticles with strong absorbance in NIR-II window for in vivo photothermal therapy and photoacoustic imaging. *Biomaterials* **2018**, *155*, 103–111.
100. Jiang, Y.; Li, J.; Zhen, X.; et al. Dual-peak absorbing semiconducting copolymer nanoparticles for first and second near-infrared window photothermal therapy: A comparative study. *Adv. Mater.* **2018**, *30*, 1705980.
101. Cao, Y.; Dou, J.-H.; Zhao, N.-J.; et al. Highly efficient NIR-II photothermal conversion based on an organic conjugated polymer. *Chem. Mater.* **2017**, *29*, 718–725.
102. Zhou, B.; Hu, Z.; Jiang, Y.; et al. Theoretical exploitation of acceptors based on benzobis (thiadiazole) and derivatives for organic NIR-II fluorophores. *Phys. Chem. Chem. Phys.* **2018**, *20*, 19759–19767.
103. Antaris, A.L.; Chen, H.; Cheng, K.; et al. A small-molecule dye for NIR-II imaging. *Nat. Mater.* **2016**, *15*, 235–242.
104. Fang, Y.; Shang, J.; Liu, D.; et al. Design, synthesis, and application of a small molecular NIR-II fluorophore with maximal emission beyond 1200 nm. *J. Am. Chem. Soc.* **2020**, *142*, 15271–15275.
105. Schnermann, M.J. Organic dyes for deep bioimaging. *Nat.* **2017**, *551*, 176–177.
106. Sun, C.; Li, B.; Zhao, M.; et al. J-aggregates of cyanine dye for NIR-II in vivo dynamic vascular imaging beyond 1500 nm. *J. Am. Chem. Soc.* **2019**, *141*, 19221–19225.
107. Ren, T.B.; Wang, Z.Y.; Xiang, Z.; et al. A general strategy for development of activatable NIR-II fluorescent probes for in vivo high-contrast bioimaging. *Angew. Chem.* **2021**, *133*, 813–818.
108. Yao, D.; Wang, Y.; Zou, R.; et al. Molecular engineered squaraine nanoprobe for NIR-II/photoacoustic imaging and photothermal therapy of metastatic breast cancer. *ACS Appl. Mater. Interfaces* **2020**, *12*, 4276–4284.
109. Zeng, X.; Xiao, Y.; Lin, J.; et al. Near-infrared II dye-protein complex for biomedical imaging and imaging-guided photothermal therapy. *Adv. Healthc. Mater.* **2018**, *7*, 1800589.
110. Zhou, H.; Zeng, X.; Li, A.; et al. Upconversion NIR-II fluorophores for mitochondria-targeted cancer imaging and photothermal therapy. *Nat. Commun.* **2020**, *11*, 6183.
111. Wang, X.; Cheng, L. Multifunctional two-dimensional nanocomposites for photothermal-based combined cancer therapy. *Nanoscale* **2019**, *11*, 15685–15708.
112. Sun, J.; Cai, W.; Sun, Y.; et al. Facile synthesis of melanin-dye nanoagent for NIR-II fluorescence/photoacoustic imaging-guided photothermal therapy. *Int. J. Nanomed.* **2020**, *15*, 10199–10213.
113. Chen, S.; Sun, B.; Miao, H.; et al. NIR-II dye-based multifunctional telechelic glycopolymers for NIR-IIa fluorescence imaging-guided stimuli-responsive chemo-photothermal combination therapy. *ACS Mater. Lett.* **2020**, *2*, 174–183.
114. Xu, Y.; Zhang, Y.; Li, J.; et al. NIR-II emissive multifunctional AIEgen with single laser-activated synergistic photodynamic/photothermal therapy of cancers and pathogens. *Biomaterials* **2020**, *259*, 120315.
115. Zhang, J.; Wang, N.; Ji, X.; et al. BODIPY-based fluorescent probes for biothiols. *Chem. Eur. J.* **2020**, *26*, 4172–4192.
116. Bai, L.; Sun, P.; Liu, Y.; et al. Novel aza-BODIPY based small molecular NIR-II fluorophores for in vivo imaging. *Chem. Commun.* **2019**, *55*, 10920–10923.
117. Godard, A.; Kalot, G.; Pliquett, J.; et al. Water-soluble Aza-BODIPYs: Biocompatible organic dyes for high contrast in vivo NIR-II imaging. *Bioconjug. Chem.* **2020**, *31*, 1088–1092.
118. Sinkeldam, R.W.; Greco, N.J.; Tor, Y. Fluorescent analogs of biomolecular building blocks: Design, properties, and applications. *Chem. Rev.* **2010**, *110*, 2579–2619.
119. Kobayashi, H.; Ogawa, M.; Alford, R.; et al. New strategies for fluorescent probe design in medical diagnostic imaging. *Chem. Rev.* **2010**, *110*, 2620–2640.
120. Willmann, J.K.; Van Bruggen, N.; Dinkelborg, L.M.; et al. Molecular imaging in drug development. *Nat. Rev. Drug Discov.* **2008**, *7*, 591–607.
121. Thekkek, N.; Richards-Kortum, R. Optical imaging for cervical cancer detection: Solutions for a continuing global problem. *Nat. Rev. Cancer* **2008**, *8*, 725–731.
122. Ma, Q.; Su, X. Near-infrared quantum dots: Synthesis, functionalization and analytical applications. *Analyst* **2010**, *135*, 1867–1877.
123. Lavis, L.D.; Raines, R.T. Bright ideas for chemical biology. *ACS Chem. Biol.* **2008**, *3*, 142–155.
124. Mishra, A.; Behera, R.K.; Behera, P.K.; et al. Cyanines during the 1990s: A review. *Chem. Rev.* **2000**, *100*, 1973–2012.
125. Li, B.; Lu, L.; Zhao, M.; et al. An efficient 1064 nm NIR-II excitation fluorescent molecular dye for deep-tissue high-resolution dynamic bioimaging. *Angew. Chem. Int. Ed.* **2018**, *57*, 7483–7487.
126. Li, T.; Li, C.; Ruan, Z.; et al. Polypeptide-conjugated second near-infrared organic fluorophore for image-guided photothermal therapy. *Acs Nano* **2019**, *13*, 3691–3702.
127. Starosolski, Z.; Bhavane, R.; Ghaghada, K.B.; et al. Indocyanine green fluorescence in second near-infrared (NIR-II) window. *PLoS ONE* **2017**, *12*, e0187563.

128. Meng, X.; Zhang, J.; Sun, Z.; et al. Hypoxia-triggered single molecule probe for high-contrast NIR II/PA tumor imaging and robust photothermal therapy. *Theranostics* **2018**, *8*, 6025.
129. Buzea, C.; Pacheco, I.I.; Robbie, K. Nanomaterials and nanoparticles: Sources and toxicity. *Biointerphases* **2007**, *2,* MR17–MR71.
130. Oliveira, M.I.; Santos, S.G.; Oliveira, M.J.; et al. Chitosan drives anti-inflammatory macrophage polarisation and pro-inflammatory dendritic cell stimulation. *Eur. Cell Mater.* **2012**, *24*, 133–136.
131. Tomić, S.; Rudolf, R.; Brunčko, M.; et al. Response of monocyte-derived dendritic cells to rapidly solidified nickel-titanium ribbons with shape memory properties. *Eur. Cell Mater.* **2012**, *23*, 58–80.
132. Lazareva, P.I.; Stupin, V.A.; Lazarev, K.A.; et al. Biodistribution and toxicological impact assessment of cerium dioxide nanoparticles in murine models: A systematic review of in vivo and ex vivo studies. *Pharmaceutics* **2025**, *17*, 1475.
133. Zhang, X.-D.; Wu, D.; Shen, X.; et al. In vivo renal clearance, biodistribution, toxicity of gold nanoclusters. *Biomaterials* **2012**, *33*, 4628–4638.
134. Luo, R.; Zhang, C.; Zhang, Z.; et al. NIR-II upconversion nanomaterials for biomedical applications. *Nanoscale* **2025**, *17*, 2985–3002.
135. Yang, S.; Li, N.; Xiao, H.; et al. Clearance pathways of near-infrared-II contrast agents. *Theranostics* **2022**, *12*, 7853.
136. Thangudu, S.; Su, C.-H. Review of light activated antibacterial nanomaterials in the second biological window. *J. Nanobiotechnology* **2025**, *23*, 293.
137. Zhang, X.D.; Chen, J.; Min, Y.; et al. Metabolizable Bi_2Se_3 nanoplates: Biodistribution, toxicity, and uses for cancer radiation therapy and imaging. *Adv. Funct. Mater.* **2014**, *24*, 1718–1729.
138. Choi, H.S.; Liu, W.; Misra, P.; et al. Renal clearance of nanoparticles. *Nat. Biotechnol.* **2007**, *25*, 1165.
139. Li, X.; Wang, B.; Zhou, S.; et al. Surface chemistry governs the sub-organ transfer, clearance and toxicity of functional gold nanoparticles in the liver and kidney. *J. Nanobiotechnol.* **2020**, *18*, 45.
140. Yu, M.; Zheng, J. Clearance pathways and tumor targeting of imaging nanoparticles. *ACS Nano* **2015**, *9*, 6655–6674.
141. Yu, S.; Xia, G.; Yang, N.; et al. Noble metal nanoparticle-based photothermal therapy: Development and application in effective cancer therapy. *Int. J. Mol. Sci.* **2024**, *25*, 5632.
142. Zhang, L.; Niu, G.; Lu, N.; et al. Continuous and scalable production of well-controlled noble-metal nanocrystals in milliliter-sized droplet reactors. *Nano Lett.* **2014**, *14*, 6626–6631.
143. Hua, S.; De Matos, M.B.; Metselaar, J.M.; et al. Current trends and challenges in the clinical translation of nanoparticulate nanomedicines: Pathways for translational development and commercialization. *Front. Pharmacol.* **2018**, *9*, 790.
144. Zhang, L.; Yang, F.; Liu, J.; et al. Exosomes in tissue engineering and cell-free therapy: A comprehensive review. *Eur. Cell Mater.* **2026**, *55*, 80–105.
145. Yang, C.; Lou, Y.; Bai, M.; et al. Advances in metal-based nanomedicine: From basic science to clinical implications. *Chin. Chem. Lett.* **2025**, *in press*.
146. Si, S.; Wu, K.; Zhang, X.; et al. Research progress of nanoparticles in the diagnosis and treatment of renal ischemia-reperfusion injury. *J. Nanobiotechnol.* **2026**, *24*, 201.
147. Hulsart-Billström, G.; Dawson, J.; Hofmann, S.; et al. A surprisingly poor correlation between in vitro and in vivo testing of biomaterials for bone regeneration: Results of a multicentre analysis. *Eur. Cell Mater.* **2016**, *31*, 312–322.
148. Shahalaei, M.; Azad, A.K.; Sulaiman, W.M.A.W.; et al. A review of metallic nanoparticles: Present issues and prospects focused on the preparation methods, characterization techniques, and their theranostic applications. *Front. Chem.* **2024**, *12*, 1398979.